DEPARTMENT OF PHYSICS, UNIVERSITY OF JYVÄSKYLÄ
RESEARCH REPORT No. 3/1987

MONTE CARLO AND MOLECULAR DYNAMICS SIMULATIONS OF NEAR-SURFACE PHENOMENA

BY
SEPPO VALKEALAHTI

Academic Dissertation
for the Degree of
Doctor of Philosophy

Jyväskylä, Finland
October 1987

URN:ISBN:978-951-39-9701-4
ISBN:978-951-39-9701-4 (PDF)
ISSN 0075-465X

Jyväskylän yliopisto, 2023

ISBN 951-679-781-4
ISSN 0075-465X

DEPARTMENT OF PHYSICS, UNIVERSITY OF JYVÄSKYLÄ
RESEARCH REPORT No. 3/1987

MONTE CARLO AND MOLECULAR DYNAMICS SIMULATIONS OF NEAR–SURFACE PHENOMENA

BY
SEPPO VALKEALAHTI

Academic Dissertation
for the Degree of
Doctor of Philosophy

To be presented, by permission of the
Faculty of Mathematics and Natural Sciences
of the University of Jyväskylä,
for public examination in Auditorium S–212 of the
University on November 21, 1987, at 12 o'clock noon.

Jyväskylä, Finland
October 1987

PREFACE

This thesis is a summary of research work carried out during the years 1983–1987 mainly at the Department of Physics in the University of Jyväskylä (Jyväskylä, Finland). Part of the work has been done in the Risø National Laboratory (Roskilde, Denmark). I present my gratitude to both of these laboratories.

I am particularly indebted to Professor Risto Nieminen for providing me an opportunity for this research work and for his competent supervision.

I want to express my gratitude to all the people with whom I have been dealing during this work. Especially I am grateful to Dr. Henrik Hansen, Dr. Jørgen Schou and Mr. Hannu Rajainmäki.

Most of all I wish to thank my wife, Kyllikki, for her forbearance and encouragement.

I am indebted to the Academy of Finland and the Risø National Laboratory for financial support. I also wish to express my gratitude to Emil Aaltonen Foundation, who has supported this work by a grant.

Jyväskylä, October 1987

Seppo Valkealahti

ABSTRACT

In this thesis, applications of the Monte Carlo and molecular dynamics simulation methods on different surface and near surface phenomena are presented. Monte Carlo simulation is used to investigate positron and electron slowing down in solid matter. The description of elastic scattering is based on accurate cross sections of effective crystalline atom potentials. Inelastic processes are described separately for each energy level by Gryzinski's excitation function. Various materials are studied and several electron and positron slowing down parameters and distributions are extracted. For example, backscattering and transmission energy and angular distributions, backscattering and transmission yields, and penetration depth and energy deposition distributions are calculated. The results are used to analyze and interprete a number of recent experiments utilizing keV electron and positron beams.

Positrons lose less energy and scatter to smaller angles than electrons when slowing down in material. This is demonstrated by several extracted parameters. In particular, the differences in elastic scattering cross sections result in some drastic differences between positrons and electrons. Positrons have larger probability to penetrate through thin films and they penetrate deeper into material than electrons. A clear consequence of the different elastic scattering cross sections for positrons and electrons is that the backscattering probability from materials is for positrons about half of that for electrons. Differences between positrons and electrons increase as a function of atomic number of the target material and decrease as a function of incident energy. The implantation profile of particles is found to be a negative of the derivative of a Gaussian function in contradiction to earlier assumptions that the profile is an exponentially decreasing function. Analytic fits are presented for the stopping profiles and their Laplace transforms as well for the

energy deposition and ionization profiles.

Molecular dynamics simulation methods are used to study (i) damage production in aluminum (110) surfaces due to low–energy argon ion bombardment and (ii) the premelting effects of solid noble gas surfaces. Appropriately constructed pair potentials were assigned between the particles, and an electronic friction term proportional to the velocity was used for energetic ions. Of particular interest in (i) are the defect and implanted atom distributions, which are compared against recent experiments. In (ii), the simulations show the equilibrium existence of liquid–like layers on the densely packed surfaces well below the bulk melting temperature.

The main results in (i) are the follows. The mean vacancy concentration depth depends only slightly on the incident angle. The total number of vacancies is almost independent of the incident ion dose for very oblique angles of incidence ($\theta > 45^\circ$). For small incident angles (near to normal) the number of vacancies per incident ion is small due to effective channeling of Ar^+ ions, but the total number of vacancies increases considerably with increasing dose. Vacancy profile is found to have a clear peak in the topmost atomic layers and a broader tail deep in the material. The interstitial and Ar^+ ion profiles are clearly deeper in the material than the vacancy profile. In (ii), a layer–by–layer premelting of Lennard–Jones (111) surfaces is observed. Also the (100) surfaces premelt, but the disordering mechanism for the loosely packed (110) surfaces is roughening. Furthermore, a general rule seems to be that melting proceeds along the directions of high packing densities.

CONTENTS

1. INTRODUCTION 1

2. MONTE CARLO SIMULATIONS OF keV POSITRON AND ELECTRON SLOWING DOWN IN SOLIDS 6

2.1. Monte Carlo Simulation Method 6

2.1.1. Elastic Scattering 7

2.1.2. Inelastic Scattering 12

2.1.3. Electronic Stopping Power 14

2.1.4. Simulation Procedure 17

2.2. Transmission through Thin Films 19

2.3. Backscattering from Solids 24

2.3.1. Normal Incidence 24

2.3.2. Oblique Incidence 30

2.4. Slowing Down in Solids 35

2.4.1. Implantation 35

2.4.2. Energy Deposition 44

2.5. Parametrization of the Stopping and Energy Deposition Profiles 50

2.5.1. Implantation Profile 50

2.5.2. Re–emission of Positrons 54

2.5.3. Energy Deposition Profile 59

3. MOLECULAR DYNAMICS SIMULATIONS OF NEAR–SURFACE PHENOMENA 63

3.1. Molecular Dynamics Simulation Method 63

3.1.1. Simulation of Damage Production by Energetic Ions 64

3.1.2. Simulation of Surface Melting 67

3.2. Damage Production in Sputtering of Al (110) Surface with Slow Argon Ions 69

3.2.1. Damage Produced by a Single Ar^+ Ion 69

3.2.2. Continuous Sputtering 73

3.3. Premelting of Noble Gas (111) Surfaces 76

3.3.1. Reliability of Thin Film Calculations 77

3.3.2. Premelting of Lennard–Jones (111) Surfaces 80

3.3.3. Discussion 87

4. SUMMARY 89

APPENDIX 91

REFERENCES 93

1. INTRODUCTION

The properties of materials can be approached from two opposite limits. In the microscopic (atomic) level electronic structure of interacting particles plays the central role. In the macroscopic scale, classical concepts and continuum models are often adequate. Between these two scales there are several interesting and often very important physical phenomena, which cannot be treated directly by extrapolating from either end. These phenomena take place in the "mesoscopic" scale between a few Ångström and a few thousand Ångströms. They are often in the extreme limits of experimental methods and therefore the existing information about them is scarce. For studying these atomic scale phenomena often the most effective tool is simulation, which is based on simplified microscopic concepts, but deals with a large number (up to several thousands) of atoms or molecules. In this thesis the Monte Carlo (MC) and molecular dynamics (MD) simulation methods are used to study atomic scale surface and near–surface phenomena.

Experimental and theoretical data about keV positrons and electrons propagating in solid matter is scarce. Theoretical calculations [He76] do exist for somewhat higher energies ($>$ 10 keV), because they are important in electron microscopy and in other areas. Also a number of experiments have been carried out for over 10 keV electrons impinging on different materials, but only few for keV electrons. The main experimental difficulty lies in producing the homogeneous thin films necessary in transmission experiments. For positrons the experimental data is lacking almost totally, because intensive monoenergetic positron beam facilities have been developed just during the last few years.

The arrival of low–energy (around 1 keV) monoenergetic positron beams (see e.g. [Mi82a]) has made it possible to perform a variety of interesting experiments. The various features of the interaction of slow positrons with matter make them

in many respects a unique surface probe. In particular the technique could be superior in providing atomistic information about lattice defects in the surface and near–surface regions and in thin films. A prerequisite for the quantitative analysis for such experiments is an accurate knowledge of the positron implantation profiles. The measurements of Mills and Wilson [Mi82b] for thin Al and Cu films gave a good starting point for estimating the mean ranges, but the reliable keV positron implantation profiles for all materials were still lacking.

Furthermore, the importance of keV electrons in materials research has increased during the past decade [Ic81]. The interaction of keV electrons with solids plays an important role in the radiation effects in fusion plasma studies, health physics, astrophysics, materials research and related topics. The properties of electron penetration in hydrogen, deuterium and tritium is generally significant for the studies of fusion plasma and plasma wall interaction and, in particular, for development of the re fuelling of future fusion reactors by the injection of a mixture of solid deuterium and tritium pellets [Ch80, Mi81]. The knowledge of electron penetration propertiers in air is crucial for the studies of the atmosphere. Also the electronic sputtering of condensed gases by charged particles has been investigated intensively during the past decade [Jo83, Be81, To83]. Despite the good knowledge of the behaviour of over 10 keV electrons in solid materials, the behaviour at keV region can not be estimated on that basis and new, unknown features can be expected at keV energies.

Here the results of full Monte Carlo simulations of the slowing down process of 1–10 keV positrons and electrons are presented. The elastic scattering is based on exact cross sections of effective crystalline potentials and the ionization processes are described by Gryzinski's semiempirical expression [Gry65] separately for each electron energy level. The excitation processes are approximated by an energy–dependent cross section so that the total electronic stopping power for electrons agrees with the Bethe formula [Be53] at high energies (10 keV). The simulations

have been terminated at 20 eV and thus the later stages of thermalization and other temperature dependent effects have been ignored.

Several kind of materials are studied from one component systems to alloys in bulk, film, and multilayer geometries. Also the incident angle of positrons and electrons is varied. The simulation sequences are used to extract the statistical distributions of overall and projected implantation profiles, energy deposition and ionization profiles, slowing down times, backscattering energy and angular distributions, total backscattering yields, transmission energy and angular distributions, total transmission yields, secondary electron emission yields and time spectra, and secondary electron emission energy and angular distributions. Here the most interesting results are presented for nitrogen, aluminum, copper, and gold (i.e. a representative set of materials), but also results for other materials are included. Parametrizations are presented for the stopping profiles as well for the ionization and energy deposition profiles. Laplace transforms of the stopping profiles should be of benefit in analyzing the re–emission data of implanted, thermalized positrons.

Sputtering of solid surfaces by particle irradiation is commonly used for sample cleaning and preparation and modification of material properties in surface science and vacuum technology [Be81, Be83]. Quantitative theoretical and experimental information has been obtained concerning the sputtering yield and distribution of sputtered particles in a variety of different conditions. The implantation profile of projectile particles can also be analyzed [Zo84]. However, the production and behaviour of irradiation–induced atomic defects are poorly understood [Mi84]. The formation of defects has a drastic effect on many physical processes associated with sputtering, e.g. selective sputtering of multicomponent systems, compositional changes at near–surface regions, irradiation–induced segregation and mixing, etc. Recently an experimental method based on the use of slow monoenergetic positron beam has been used to study damage production in Al (110) surface with Ar^+ ion

bombardment [Ve85, Mä86].

In the past, mainly Monte Carlo –type (to a lesser extent molecular dynamics simulation) methods have been used to study processes associated with material bombardment with energetic ions. Simulations have been performed for different incident ion and target material combinations. Collision cascades, displacements, damage production, recombination, incident ion ranges, and ejection of surface atoms have been investigated [An87, Bi84, Sh85, Is74, Ja86, Er65, Web83, Ha83a, Ha83b, Si86]. However, the knowledge of the damage production associated with sputtering of metal surfaces with low–energy ions has been inadequate.

Here both the maximum damage production per an Ar^+ ion incident on a perfect aluminum lattice and a continuous sputtering of Al (110) surface by Ar^+ ions are simulated by molecular dynamics method. The sputtering yield and the overall shape and the mean depth of the vacancy, interstitial, and projectile profiles are extracted for 200 and 400 eV Ar^+ ions and for different angles of incidence. Simulations are continued until the energy of the fastest atom is below the displacement threshold energy and thus the maximum rate of damage production is monitored. Also the recovery of the sample after a continuous sputtering is followed.

The last subject of this thesis is the premelting of noble gas surfaces. The structure of crystal surfaces close to but below the bulk melting temperature has been discussed widely during the past decade. Especially the occurrence of premelting phenomena has been investigated intensively [Li82, Li84, Li86, Br78, Br83a, Br83b, Po85, Ro86, Sc85, Ja85, Ho85, La86, Fr85, Fr86]. For example, Lipowsky [Li82, Li84, Li86] has given general arguments about surface phenomena at the first order bulk transitions. Frenken *et al.* [Fr85, Fr86] have observed the presence of a liquid surface film on top of a well ordered Pb (110) substrate below the bulk melting temperature. Broughton *et al.* [Br78, Br83a, Br83b] have predicted the premelting of Lennard–Jones (LJ) surfaces by molecular dynamics simulation, and

on the contrary Rosato *et al.* [Po85, Ro86] have shown by a more detailed MD simulation that the disordering mechanism below the bulk melting point for LJ (110) surfaces is surface roughening. Nevertheless, no general agreement exists about whether real premelting of surface layers takes place or merely disordering (roughening) is the dominating mechanism.

Here the premelting of Lennard–Jones (111) surfaces has been studied in more detail by molecular dynamics methods. Surface premelting has been analyzed by means of total energies, trajectory plots, mean square displacement functions, diffusions coefficients, vacancy concentrations, and two dimensional order parameters. Premelting of the (111) surface layers is observed far below the bulk melting temperature and a complete view of the disordering of LJ-surfaces below the bulk melting temperature is obtained.

This thesis is based on and complements the following publications:

1. **S. Valkealahti** and R. M. Nieminen: Monte Carlo Calculations of keV Electron and Positron Slowing Down in Solids, Appl. Phys. A **32** (1983) 95–106. https://doi.org/10.1007/BF00617834
2. **S. Valkealahti** and R. M. Nieminen: Monte Carlo Calculations of keV Electron and Positron Slowing Down in Solids. II, Appl. Phys. A **35** (1984) 51–59. https://doi.org/10.1007/BF00620300
3. **S. Valkealahti**, J. Schou, H. Sørensen and R. M. Nieminen: Range and Stopping Power of keV Electrons in Solid Hydrogens, J. Appl. Phys., to be published. https://doi.org/10.1016/0168-583X(88)90052-3
4. **S. Valkealahti**, J. Schou, and R. M. Nieminen: Energy Deposition of keV Electrons in Light Materials, to be published. https://doi.org/10.1063/1.342839
5. A. Vehanen, J. Mäkinen, P. Hautojärvi, H. Huomo, J. Lahtinen, R. M. Nieminen, and **S. Valkealahti**: Near–Surface Defect Profiling with Slow Positrons: Argon–Sputtered Al (110), Phys. Rev. B **32**, Rapid Comm. (1985) 7561–7563. https://doi.org/10.1103/PhysRevB.32.7561
6. J. Mäkinen, A. Vehanen, P. Hautojärvi, H. Huomo, J. Lahtinen, R. M. Nieminen, and **S. Valkealahti**: Vacancy–Type Defect Distributions Near Argon-Sputtered Al (110) Surface Studied by Variable–Energy Positrons and Molecular Dynamics Simulations, Surf. Sci. **175** (1986) 385–414. https://doi.org/10.1016/0039-6028(86)90242-6
7. **S. Valkealahti** and R. M. Nieminen: Molecular Dynamics Simulation of the Damage Production in Al (110) Surface with Slow Argon Ions, Nucl. Inst. Meth. B **18** (1987) 365–369. https://doi.org/10.1016/S0168-583X(86)80060-X
8. **S. Valkealahti** and R. M. Nieminen: Molecular Dynamics Investigation of the Premelting Effects of Lennard–Jones (111) Surfaces, Physica Scripta **36** (1987) 646–650. https://doi.org/10.1088/0031-8949/36/4/007

2. MONTE CARLO SIMULATIONS OF keV POSITRON AND ELECTRON SLOWING DOWN IN SOLIDS

2.1. MONTE CARLO SIMULATION METHOD

The main ideas of Monte Carlo simulation of collision cascades are well known (see e.g. [He76]). Also, the present electron and positron slowing down simulation procedure has been outlined earlier [Va83, Va84]. However, it has been improved upon and the full scheme is presented here. A schematic view on positron and electron processes in material is shown in Fig. 1.

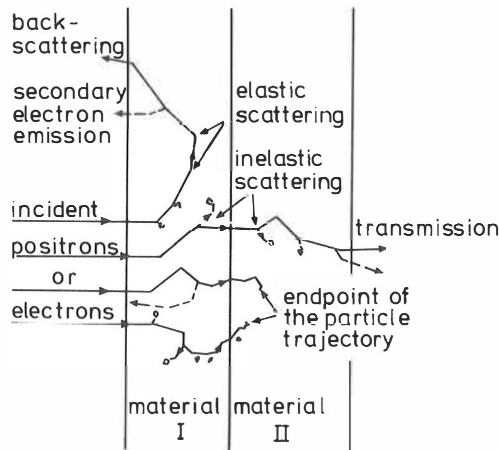

Fig. 1. Schematic drawing of the positron (electron) processes in material.

In the present approach the elastic scattering processes are calculated using accurate atomic cross sections, which have been modified to include approximately

the effect of lattice structure. The ionization processes are calculated separately for each target electron energy level using Gryzinski's excitation function [Gry65]. The energy dependence of the cross section for the excitation processes is approximated by a "rectangular" form (Fig. 5) so that the total stopping power of electrons agrees with the Bethe formula [Be53] at high energies.

The Monte Carlo simulation program is developed for simulation of numerous different situations. Several kind of materials can be studied from one component systems to alloys. Bulk, film, and various multilayer geometries are possible. Also the incident angle of projectiles can be varied. The simulation sequences are used to extract the statistical distributions of overall and projected implantation ranges, the ionization and energy deposition distributions, slowing down times, backscattering energy and angular distributions, total backscattering yields, transmission energy and angular distributions, total transmission yields, secondary electron emission yields and time spectra, and secondary electron energy and angular distributions.

In the following the adapted elastic and inelastic scattering processes are described as well the connection to the electronic stopping power. Finally the simulation procedure is briefly described.

2.1.1. Elastic Scattering

The differential scattering cross section for a spherical potential can be calculated from the partial wave sum [Me63]

$$\frac{d\sigma(E,\theta)}{d\Omega} = \frac{1}{k^2}\left|\sum_{l=0}^{\infty}\left[(2l+1)e^{i\delta_l}\sin\delta_l P_l(\cos\theta)\right]\right|^2, \qquad (1)$$

where k is the wave number, δ_l the phase shift of the lth partial wave and θ the polar scattering angle from the initial direction. The Legendre functions P_l can

be effectively generated using their recurrence relation [Gra65]. The phase shifts are obtained by solving the radial Schrödinger equation

$$\left[-\frac{d^2}{dr^2} + \frac{2\mu}{\hbar}V(r) + \frac{l(l+1)}{r^2} - k^2\right] u_{l,k} = 0 \tag{2}$$

numerically by Milne's method [Ab65] and matching the solution to the asymptotic form $\sin(kr - l\pi/2 + \delta_l)$. Above μ is the reduced mass, r the distance from the atomic center, $u_{l,k}$ the lth wavefunction and $V(r)$ the effective single–atom potential in condensed matter.

The total elastic scattering cross section is obtained by integrating (1) over angles as

$$\sigma_{el}(E) = 2\pi \int_0^\pi \frac{d\sigma(E,\theta')}{d\Omega} \sin\theta' d\theta'. \tag{3}$$

The effective single atom scattering potential $V(r)$ is evaluated as follows. Firstly, a free atom potential and electron density are calculated selfconsistently by the density–functional method [Ho64, Ko65, Gu76]. Secondly, approximations for the crystalline charge density and Coulomb (electrostatic) potential are built up by superimposing atomic charge densities and potentials in a lattice. The spherical average of the charge density and Coulomb potential around an atom are then evaluated. Thirdly, the exchange and correlation between electrons are included by adding a local–density–dependent exchange–correlation potential [Gu76] to the Coulomb potential. For positrons, only the spherical average of the Coulomb potential with the reversed sign is included. The scattering potentials are normalized to zero at the Wigner–Seitz radius. Equation (2) is then solved for each partial wave by numerical integration. The number of partial waves, which contribute (in practice) to the elastic scattering cross section, is a few for eV energies and increases up to 50 for 10 keV particles, depending on the target material. Inserting the calculated phase shifts in (1) and (3) the differential and the total elastic scattering cross section can be obtained separately for electrons and positrons.

For the collision cascade simulations the differential elastic scattering cross sections ($d\sigma(E,\theta)/d\Omega$–data) were evaluated for discrete values of energy and angle from 1 eV to 10 keV and from 0 to 180 degrees, respectively. During the simulation, the differential scattering cross section for an arbitrary value of the incident particle energy is interpolated from the calculated data set. The scattering angle θ is determined by selecting a uniform random number $0 \leq R_1 \leq 1$ and finding a value of θ which satisfies

$$R_1 = 2\pi \int_0^{\theta} \frac{d\sigma(E,\theta')}{d\Omega} \sin\theta' d\theta' \Big/ \sigma_{el}(E). \tag{4}$$

The azimuthal scattering angle is selected randomly from a uniform angular distribution.

It is crucial for keV electron and positron collision cascade simulations to treat elastic scattering processes accurately. At energies above 10 keV the elastic scattering cross section is described reasonably well by formulas representing the "screened" Rutherford scattering cross section [Ni59]. At keV energies these semiempirical formulas fail (usually overestimate, Fig. 2) in describing elastic scattering processes. Also both the differential and total elastic scattering cross sections are distinctly different for electrons and positrons.

Electrons generally have larger total elastic scattering cross section than positrons as is shown for copper in Fig. 2. The difference between electrons and positrons decreases as a function of energy and increases as a function of atomic number. At low electron energies the elastic scattering may show a resonant behaviour and the total scattering cross section may actually be smaller than the positron cross section (Figs. 2 and 3). Larger elastic scattering cross sections for electrons result from two different phenomena. Firstly, electrons encounter an attractive potential, which increases the large angle scattering probability, whereas positrons encounter a repulsive potential. Secondly, the exchange–correlation

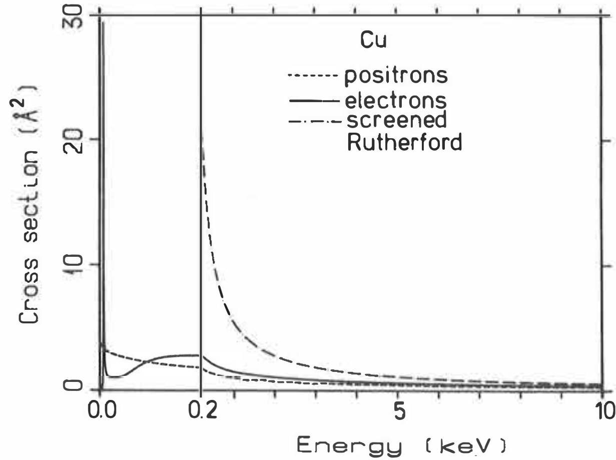

Fig. 2. Total elastic scattering cross section of positrons and electrons for a copper crystal atom.

potential increases the atomic potential relatively most in the outer region, which increases the small angle scattering probability.

Another important difference between electrons and positrons appears in the differential scattering cross section. Electrons have a larger probability to scatter into large angles ($\theta > 30^o$) than positrons, especially at small energies (Fig. 3). Due to the attractive interaction between an electron and an atom, electrons have scattering lobes into large angles. These lobes are also discernible at keV energies, although they are smaller than the line width in Fig. 4. At keV energies electrons generally have a larger probability to scatter into small angles than positrons (Fig. 4) and the total elastic scattering probability is also larger. At low energies the large angle scattering together with the larger total elastic scattering cross section causes the differences between electron and positron backscattering yields (Figs. 11–14). Differences in the forward scattering are fairly unimportant for

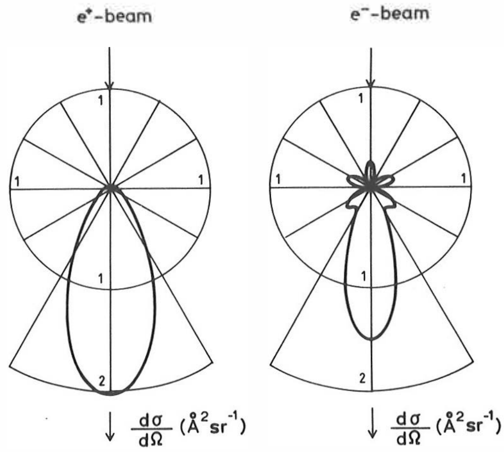

Fig. 3. Polar plot of the differential elastic scattering cross section of 100 eV positrons and electrons off a copper crystal atom.

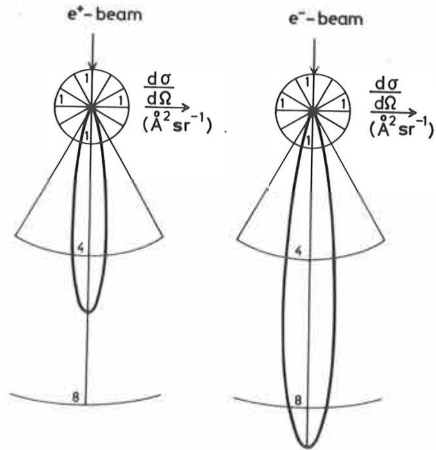

Fig. 4. Polar plot of the differential elastic scattering cross section of 1 keV positrons and electrons off a copper crystal atom.

slowing down, because the elastic forward scattering does not affect the penetration properties. Over keV energies differences in the overall shapes of the differential elastic scattering cross section and the total elastic scattering cross section between electrons and positrons decrease as functions of energy, which is seen as a decrease of differences in electron and positron slowing down properties.

2.1.2. Inelastic Scattering

At high energies positrons and electrons lose their energy mainly in inelastic collisions with core and valence electrons. These collision processes lead either to ionization or excitation of the target atom electrons. Ionization processes can be described in terms of Gryzinski's excitation function [Gry65]. For a target electron shell denoted by i the differential inelastic scattering cross section is written as

$$\frac{d\sigma_i(E,\Delta E)}{d(\Delta E)} = \frac{\pi e^4 N_i}{(\Delta E)^3}\frac{E_{B_i}}{E}\left(\frac{E}{E+E_{B_i}}\right)^{3/2}\left(1-\frac{\Delta E}{E}\right)^{E_{B_i}/(E_{B_i}+\Delta E)} \cdot\left\{\frac{\Delta E}{E_{B_i}}\left(1-\frac{E_{B_i}}{E}\right)+\frac{4}{3}\ln\left[2.7+\left(\frac{E-\Delta E}{E_{B_i}}\right)^{1/2}\right]\right\}, \quad (5)$$

where N_i, ΔE, E_{B_i}, and E are the number of electrons in shell i, the energy loss of the incident electron, the mean electron binding energy in shell i and the primary projectile energy, respectively.

To include also the excitation processes the following approximation is used

$$\left.\frac{d\sigma_i(E,\Delta E)}{d(\Delta E)}\right|_{E_{TH_i}\leq\Delta E\leq E_{B_i}} = \left.\frac{d\sigma_i(E,\Delta E)}{d(\Delta E)}\right|_{\Delta E=E_{B_i}}, \quad (6)$$

where E_{TH_i} is the threshold energy for excitation processes associated with shell i. The electron stopping cross section is fitted to agree with the Bethe formula [Be53] at high energies (10 keV) by adjusting the excitation threshold energies E_{TH_i} (Sect. 2.1.3.). The inelastic scattering cross section is shown schematically in Fig. 5.

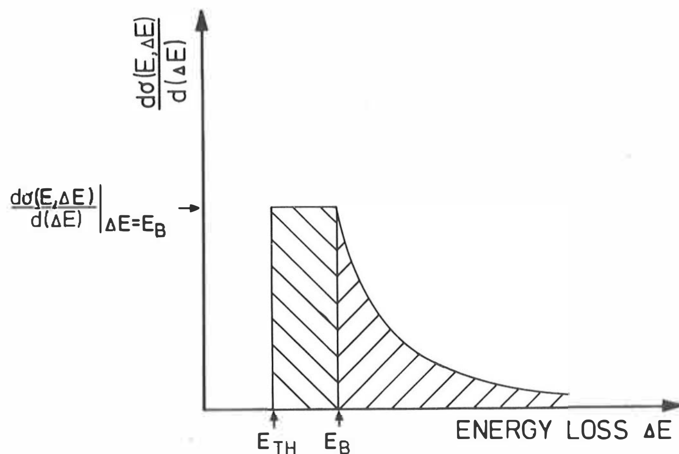

Fig. 5. Schematic drawing of the excitation function used for the inelastic processes. The shaded area under the curve to the right of E_B is the Gryzinski's ionization cross section for electrons. The shaded area to the left of E_B is the excitation cross section.

The total inelastic scattering cross section for shell i is

$$\sigma_{inel,i}(E) = \int_{E_{TH_i}}^{E} \frac{d\sigma_i(E, \Delta E)}{d(\Delta E)} d(\Delta E). \tag{7}$$

The total inelastic scattering cross section for an atom is obtained by summing over all contributing electron states m,

$$\sigma_{inel}(E) = \sum_{i=1}^{m} \sigma_{inel,i}(E). \tag{8}$$

At each inelastic scattering event the energy loss is calculated by selecting a uniform random number R_2 and then finding a value of ΔE which satisfies

$$R_2 = \int_{\Delta E}^{E} \frac{d\sigma_i(E, \Delta E')}{d(\Delta E')} d(\Delta E') \Big/ \sigma_{inel,i}(E), \tag{9}$$

where the energy loss is between $E_{TH_i} \leq \Delta E \leq E$. For electrons the most energetic particle is followed as the primary particle after the collision of two indistinguishable particles [Ro54]. Positron, of course, is followed all the time

as the primary particle. For electrons, for example, the mean penetration depth increases up to 5 % , because the most energetic electron is followed after the collision.

The scattering angle θ after an inelastic collision is obtained from the binary collision approximation [Gry65]

$$\sin\theta = (\Delta E/E)^{1/2}. \tag{10}$$

For secondary electrons it is, respectively,

$$\sin\theta' = (1 - \Delta E/E)^{1/2}. \tag{11}$$

The azimuthal scattering angle is again selected randomly from a uniform angular distribution.

2.1.3. Electronic Stopping Power

The energy loss of keV electrons and positrons is mainly caused by collisions with electrons in a solid. The total electronic stopping power $Q(E)$ for an electron with energy E is defined as

$$Q(E) \equiv -\frac{dE}{dx} = NS(E), \tag{12}$$

where N is the number density of target atoms and $S(E)$ the stopping cross section of an atom. For high incident velocities (over 10 keV) the atomic stopping cross section for an electron–electron interaction is quite accurately determined by Bethe's formula [Be33, Be53]

$$S_B(E) = \frac{2\pi Ze^4}{E}\ln\left(\frac{1.1658E}{I}\right), \tag{13}$$

where Z is the atomic number of the solid and I the mean ionization potential. The lower limit for the applicability of the Bethe stopping power is proportional

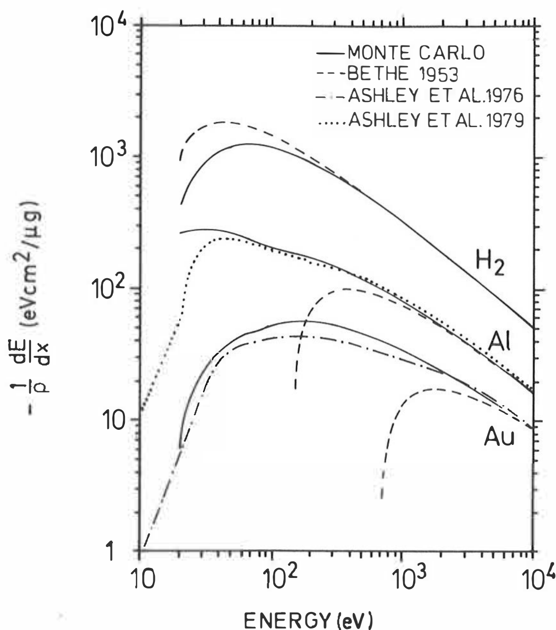

Fig. 6. The electronic stopping powers of electrons in H_2, Al, and Au.

to the mean ionization energy. For example, for gold it is valid only at energies above 10 keV, but for hydrogen down to 0.5 keV. Stopping powers for H_2, Al, and Au are shown in Fig. 6.

The total stopping cross section due to electron–electron interactions can be derived from Eq. (5) by

$$S(E) = \sum_{i=1}^{m} \int_{E_{TH_i}}^{(E+E_{B_i})/2} \Delta E \frac{d\sigma_i(E,\Delta E)}{d(\Delta E)} d(\Delta E). \tag{14}$$

The upper limit of the integration is $(E + E_{B_i})/2$, because the most energetic particle is followed after the collision of two indistinguishable particles [Ro54]. This stopping cross section for electrons has been fitted to agree with the Bethe formula (Eq. (13)) at high energies (10 keV) by adjusting the excitation threshold

energies E_{TH_i}. The threshold energies with a constant ratio E_{TH_i}/E_{B_i} for all electron levels i of an atom are used both for electrons and positrons. The ratios for the studied materials have been presented in Table 1.

Table 1. Basic data for the calculations. Z is the atomic number, I the mean ionization energy [Si75, Be82, IC84], ρ the mass density, and a the lattice constant. The electron configuration is the one included in inelastic processes, but for the lattice potential calculation the full atomic potential is used [Fr76, No73, Wea83].

Material	Z	I [eV]	E_{TH}/E_B	ρ [g/cm^2]	a [Å]	Electron configuration
H_2	1	18.3	0.50	0.089	3.75	1s
N_2	7	88.0	0.72	1.03	4.039	$1s^2 2s^2 2p^3$
Ne	10	137.0	0.81	1.56	4.43	$1s^2 2s^2 2p^6$
Al	13	163.0	0.77	2.70	4.05	$1s^2 2s^2 2p^6 3s^2 3p^1$
Si	14	173.0	0.76	2.33	5.43	$1s^2 2s^2 2p^6 3s^2 3p^2$
Ar	18	190.0	0.65	1.78	5.26	$1s^2 2s^2 2p^6 3s^2 3p^6$
Cu	29	320.0	0.84	8.90	3.61	$2s^2 2p^6 3s^2 3p^6 3d^{10} 4s^1$
W	74	727.0	0.80	19.3	3.16	$3s^2 3p^6 ... 5p^6 5d^4 6s^2$
Au	79	771.0	0.75	19.3	4.08	$3s^2 3p^6 ... 5p^6 5d^{10} 6s^1$

2.1.4. Simulation Procedure

The simulation procedure for a one–component material is presented here. Generalization to alloys is straightforward.

The mean free path λ_i, which corresponds to a collision process i of a penetrating particle, is

$$\lambda_i = \frac{A}{N_A\,\rho\,\sigma_i}, \tag{15}$$

where A, N_A, ρ, and σ_i are the atomic mass, the Avogadro constant, the mass density, and the collision cross section for process i, respectively. The inverse of the total mean free path is a sum over the inverses of different mean free paths

$$\frac{1}{\lambda_T} = \sum_{i=1}^{m+1} \frac{1}{\lambda_i}. \tag{16}$$

The summation includes both the elastic mean free path and the inelastic mean free paths.

The distance L travelled between collisions is obtained from

$$L = -\lambda_T \ln R_3, \tag{17}$$

where R_3 is a uniform random number. Another random number R_4 is used to determine the type (j) of the scattering event:

$$0 \le \lambda_T \sum_{i=1}^{j} \frac{1}{\lambda_{i-1}} \le R_4 \le \lambda_T \sum_{i=1}^{j} \frac{1}{\lambda_i} \le 1, \tag{18}$$

where $1/\lambda_0 = 0$.

The energy loss rate for an electron (positron) is largest at energies around 100 eV (Fig. 6). Electrons at these energies also have the largest probability to scatter into large angles. When the projectiles have slowed down to energies around 100 eV, they have a rather isotropic direction distribution, they wander inside a relatively small volume, and slow down quickly. Therefore the choice of the

termination energy does not have much effect. For example, the effect of changing the termination energy from 20 to 100 eV in the case of 1 keV electrons incident on Al is less than 6 % on the mean total path length and the backscattering probability and around 1 % on the mean penetration depth. In all calculations the termination energy of 20 eV is used.

During the slowing down of projectiles energetic secondary electrons are produced. In experiments it is impossible to distinguish primary and secondary electrons from each other. The calculated secondary electron emission yield can be up to 20 % of the primary electron backscattering yield. However, it depends strongly on the experimental set–up, in particular on the grid voltage. In this work only the primary electrons are considered unless otherwise noted.

2000 particle histories are used in each calculation and the statistical accuracy, for example, of the calculated backscattering, transmission, and absorption probabilities is around ± 3 %. One particle history typically contains a few hundred scattering events and the real slowing down time is of the order of 10^{-14} s. One simulation of 2000 incident particles takes typically a couple of minutes CPU time in a VAX–8600 computer, depending strongly on the projectile incident energy and on the target material. The program includes over two thousand fortran lines and the peak working set size is around one thousand kilobytes. A reduced flow chart of the MC–program is presented in the appendix.

2.2. TRANSMISSION THROUGH THIN FILMS

There are two types of basic experimental data, which can be used for direct comparison between Monte Carlo simulations and experimental results at keV energies. Firstly, particle backscattering probabilities (η_B) from semi-infinite solids have been measured for keV electrons incident on numerous materials. These comparisons are discussed in the next chapter. Secondly, keV electron and positron transmission probabilities (η_T) through thin films have been measured for several materials.

Transmission experiments are mostly performed for metals, because it is easiest to prepare unsupported thin enough films from them. Experimental transmission probability vs. film thickness data both for electrons and positrons exist only for Al and Cu [Vy67, Vy76, Vy73b, Mi82b]. These experimental results are not fully accurate because of the experimental difficulties. Anyhow, an overall view of electron and positron transmission probabilities through Al and Cu films is quite consistent. Comparisons with these data are presented here. Agreement with experimental electron data for other materials has also been observed [Sc78, Ad80, Sø78a, Øh85, Vy58]. In particular, the agreement with indirect experimental transmission data for light materials (H_2, N_2, O_2, and CO) [Sc78, Ad80, Sø78a, Øh85] confirms the usefulness of the present approach for all materials.

The simulated transmission probabilities as a function of incident projectile energy through thin Al and Cu films are presented in Figs. 7 and 8, respectively. Comparisons have been made with experimental electron [Vy67, Vy73b, Vy76] and positron [Mi82b] transmission data. The overall agreement between Monte Carlo and experimental transmission probabilities is very good both for electrons and positrons. Only at high energies (6.2 keV) the simulated positron transmission probability is somewhat higher than the experimental one [Mi82b]. Electron

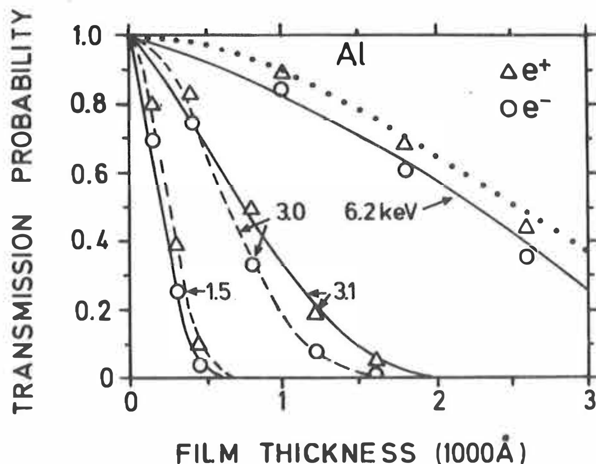

Fig. 7. Transmission probability vs. aluminum film thickness for 1.5, 3.1, and 6.2 keV positrons and 1.5, 3.0, and 6.2 keV electrons. The solid lines are experimental positron thin film transmission data [Mi82b] and the dashed and dotted lines are experimental electron thin film transmission data of [Vy67] and [Vy76], respectively.

transmission probabilities are smaller than positrons. This is due to the larger elastic scattering cross section of electrons (Fig. 2). Only the experimental transmission probabilities of Vyatskin and Trunev [Vy67] for 6.2 keV electrons from Al are clearly higher than those for positrons [Mi82b], but these authors have also obtained longer mean penetration ranges in that experiment than in others of the same group [Vy73b, Vy76].

The transmission energy distributions for 3.1 keV positrons from aluminum and copper films of different thicknesses are shown in Figs. 9 and 10, respectively. The behaviour for different film thicknesses is quite similar for positrons and electrons. As expected, positrons lose more energy in thick films than in thin films and the transmission energy distribution is also wider for thick films. Positrons lose slightly less energy than electrons in thin films. This is, again, due to the larger elastic scattering probabilities of electrons. Thus, electrons travel a longer path in

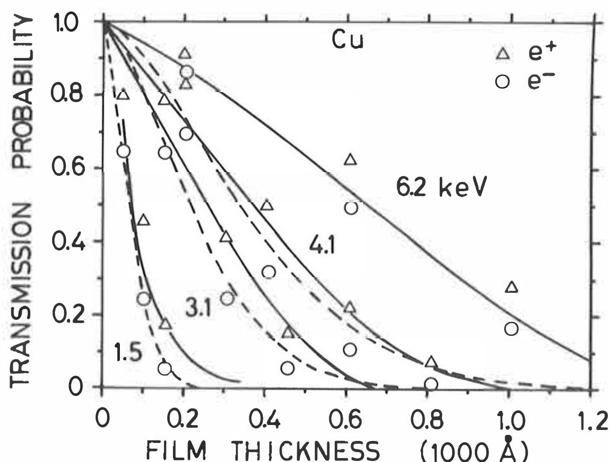

Fig. 8. Transmission probability vs. copper film thickness for 1.5, 3.1, 4.1, and 6.2 keV positrons and electrons. The solid and dashed lines are experimental positron [Mi82b] and electron [Vy73b] thin film transmission data, respectively.

the film before transmission and have higher probability to lose energy in inelastic collision than positrons. Electrons and positrons have quite high probability to go through thin heavy material films without losing much energy, whereas in light elements they lose more energy in the same mass thickness.

The transmission probability vs. film thickness data can be used to estimate particle stopping profiles from experiments. Stopping profiles, calculated from experiments, are usually taken to be the negative derivatives of the transmission probability vs. film thickness curves. This gives only a crude estimate of the stopping profile in a true semi-infinite target. One defect is that the procedure does not take into account the backscattering effect from the film. Backscattering has an important effect on the profile considerations especially for thin targets.

If the transmission (η_T) and backscattering (η_B) probabilities have been measured for different film thicknesses z_f, the stopping profiles $P(z)$ can be calculated

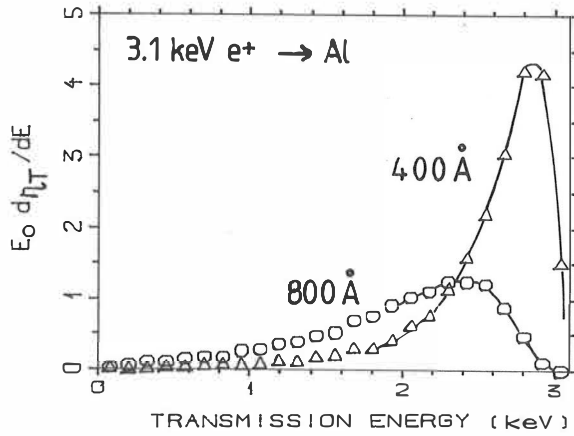

Fig. 9. Transmission energy distribution of 3.1 keV positrons for two aluminum film thicknesses. The lines are drawn just to guide the eye.

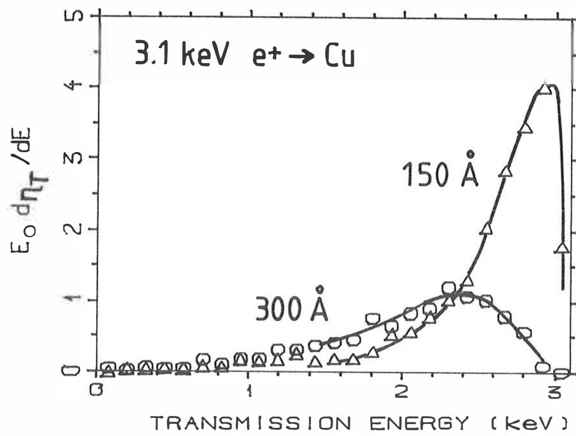

Fig. 10. Transmission energy distribution of 3.1 keV positrons for two copper film thicknesses. The lines are drawn just to guide the eye.

quite precisely as follows [Ha83]

$$P(z = z_f) \simeq \frac{d\eta_A}{dz_f} = -\frac{d\eta_T}{dz_f} - \frac{d\eta_B}{dz_f}, \tag{19}$$

where f denotes film geometry and η_A is the absorption probability. There is still at least one source of uncertainty. If we imagine a plane in semi–infinite matter perpendicular to the z–direction, a particle which goes through the plane can scatter back and thus it can cross the plane twice or even more times, whereas particles transmitted through a thin film are lost at once. This phenomenon leads to an overestimation of the penetration in a semi–infinite target when thin film transmission data is used. This can, at least partly, be taken into consideration by experimental arrangement. Mills and Wilson [Mi82b] estimated the return probability to be less than 15% for energies $E_0 < 6$ keV in Cu and Al. Nevertheless, clear differences are observed when they are compared with simulated "real" implantation profiles in semi–infinite materials (Chapter 2.4.1.).

2.3. BACKSCATTERING FROM SOLIDS

2.3.1. Normal Incidence

The backscattering probability from solids is the second and perhaps more accurate quantity for direct comparison between the Monte Carlo simulations and experimental results. A reasonable set of experimental electron backscattering data exist for various materials. Also very interesting differences are observed in MC simulations between positron and electron backscattering probabilities.

Positrons have a much smaller probability to scatter back from semi–infinite targets than electrons (Figs. 11–14). The difference between electrons and positrons increases as a function of atomic number (Figs. 11 and 12). Electrons at 1 keV have more than twice as large a backscattering probability as positrons. The difference is largest for small energies and decreases as a function of energy (Figs. 13 and 14). The reason lies again in the elastic scattering cross section of crystal atoms for positrons and electrons. Electrons have a relatively larger probability to undergo large angle scattering events, whereas positrons almost always scatter by less than 30° (Fig. 3). Positrons also have a smaller total elastic scattering cross section than electrons (Fig. 2), which, of course, decreases the overall positron backscattering probability.

For light elements the backscattering probability of electrons decreases as a function of energy whereas for heavy elements it increases (Figs. 13 and 14). The reason is that light elements have relatively larger scattering probability to large angles (backscattering lobes) than heavy elements. It decreases in magnitude with increasing energy. For heavy elements the probability distribution of scattering to different angles remains very similar at these energies. Therefore, the backscattering probability from heavy elements increases, because the number of elastic

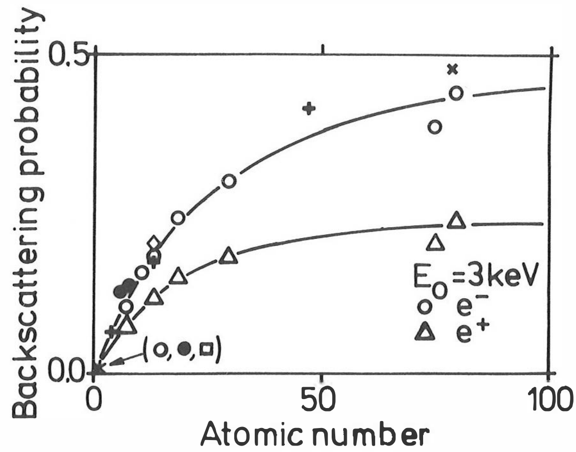

Fig. 11. Backscattering probability of 3 keV projectiles as a function of atomic number of the target material. Experimental electron data: ◇ [Fi74], ● [Sø78a], + [Vy76], × [Sc78], and □ [Sø78b]. The lines are drawn just to guide the eye.

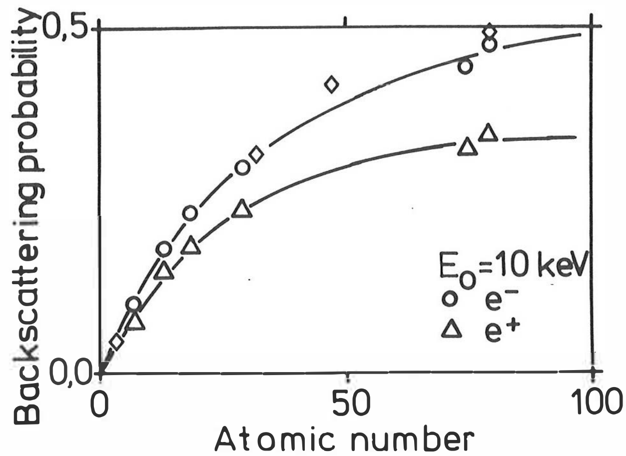

Fig. 12. Backscattering probability of 10 keV projectiles as a function of atomic number of the target material. Experimental electron data: ◇ [Fi74]. The lines are drawn just to guide the eye.

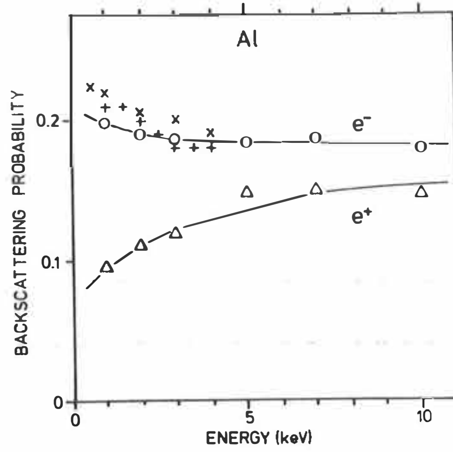

Fig. 13. Backscattering probability as a function of the incident energy from semi–infinite aluminum. The crosses and pluses are experimental electron reflection coefficients of Fitting *et al.* [Fi74] and Vyatskin *et al.* [Vy76], respectively. The lines are drawn just to guide the eye.

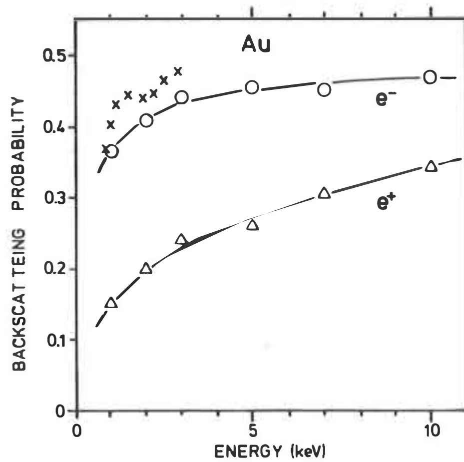

Fig. 14. Backscattering probability as a function of the incident energy from semi-infinite gold. The crosses are experimental electron reflection coefficients of Schou *et al.* [Sc78]. The lines are drawn just to guide the eye.

collisions per incident electron increases as a function of energy. At energies above 10 keV the backscattering probability begins to decrease also for heavy elements, because the total elastic scattering cross section decreases as a function of energy.

Comparison between simulated and experimental electron backscattering coefficients shows fair agreement (Figs. 11–14). The differences between the experimental and the MC coefficients are smaller than the effects of different experimental setups. In many cases these differences are most probably due to energetic secondary electrons. Their contribution can typically be of the order of 10 % (Fig. 20 and [Sh83]).

The backscattering probability of positrons increases as a function of energy for all elements. At energies above 10 keV it saturates and gradually starts to decrease similarly as for electrons. Positrons scatter only to small angles at all energies and they have to undergo several elastic collisions before they can escape from the material. At small energies most positrons have already slowed down to eV energies (where they can effectively be trapped at lattice defects) before enough elastic collisions for backscattering have taken place. The number of elastic collisions per incident positron increases as a function of energy, which increases the backscattering probability. On the other hand, the total elastic scattering cross section decreases as a function of energy, which decreases the backscattering probability at energies above 10 keV.

The backscattering energy distribution of projectiles impinging on a semi–infinite material is different for different energies (Fig. 15). The backscattering energy distribution of 2 keV electrons from Cu has its maximum peak near the initial energy, whereas the distribution of 7 keV electrons is flatter. This is due to the fact that slow electrons have a larger probability to scatter from an atom into large angles than fast electrons. 2 keV positrons have their maximum at energies ~80 % of the initial energy. At higher energies the maximum shifts to smaller ene-

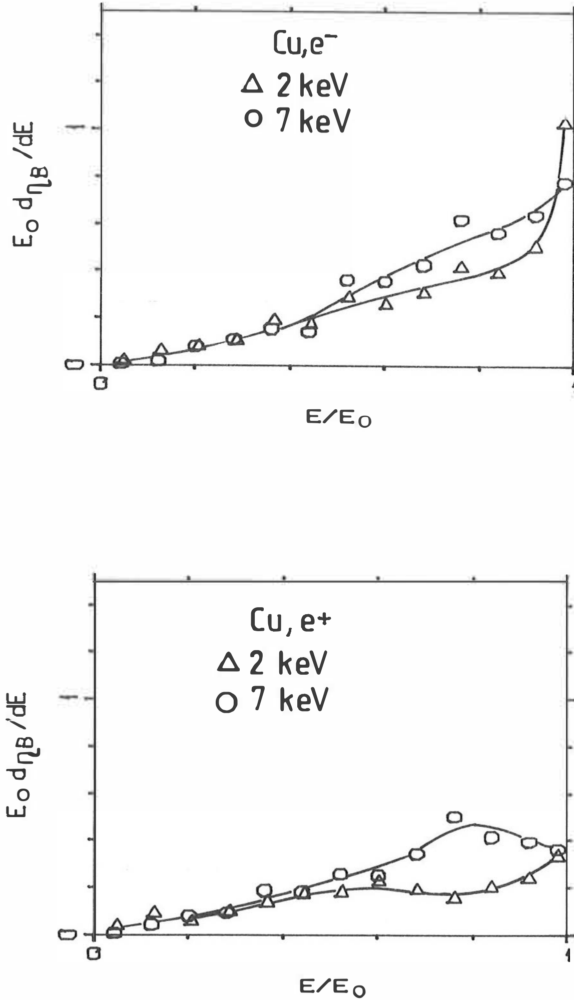

Fig. 15. Backscattering energy distribution of 2 and 7 keV electrons (above) and positrons (below) from semi-infinite Cu. The lines are drawn just to guide the eye.

rgies and disappears gradually. Positrons have their maximum at smaller energies than electrons, because of the smaller large angle scattering probability.

The maximum of the backscattering energy distribution from heavy elements is at higher energies than in the case of light materials. The reason for this is

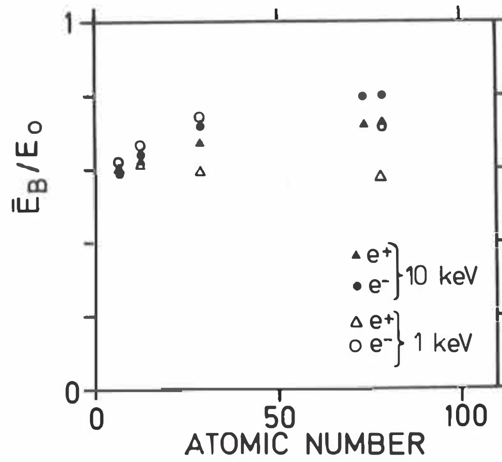

Fig. 16. The mean backscattering energy ($\overline{E}_B/E_0$) vs. the atomic number of the target material for 1 and 10 keV projectiles.

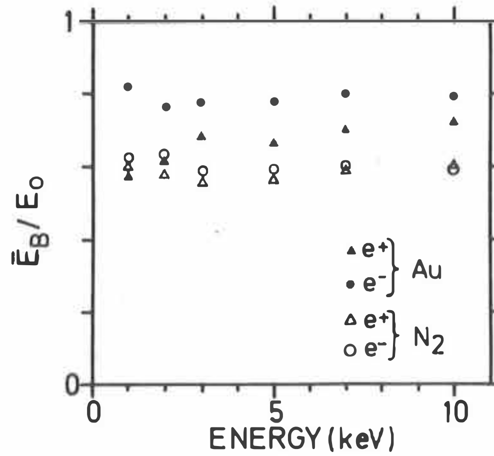

Fig. 17. The mean backscattering energy ($\overline{E}_B/E_0$) as a function of the incident energy for N_2 and Au.

that heavier atoms have larger elastic scattering cross sections. Also the mean backscattering energy E_B increases in proportion to the incident energy E_0 gradually as a function of target atomic number Z. The reason is that the elastic collision probability increases with respect to the inelastic one as a function of atomic number. The mean backscattering energy E_B is higher for electrons than for positrons. E_B is almost the same for positrons and electrons impinging on a light material at energies between 1 and 10 keV (Figs. 16 and 17). The differences between positron and electron mean backscattering energies increase as a function of atomic number Z (Fig. 16) and decrease as a function of incident energy (Fig. 17).

The reason for larger mean backscattering energies for electrons is again that they have a larger probability to scatter into large angles than positrons. Also the total elastic scattering cross section is larger for electrons than for positrons and the difference increases as a function of atomic number and decreases as a function of energy. Thus the backscattered electrons have more probably suffered large angle scattering events, whereas positrons have encountered several small angle scatterings and have lost more energy during their longer traversed path in the material.

2.3.2. Oblique Incidence

The effect of changing the incident angle is only little larger for positrons than for electrons, for example in the backscattering probability and in the penetration depth (Figs. 18, 19, and 28). Generally the electron–positron differences decrease with increasing angle and their behaviour is qualitatively similar as a function of the incident angle ϕ. The most prominent effect due to changing the angular incidence is on the backscattering probability (Fig. 18). It is almost constant between 0° and 30°, but increases rapidly at larger angles. Only about half of

the particles absorbed in the material on normal incidence are absorbed when the angle of incidence is 80°. The backscattering probability as a function of energy increases relatively more for the normal incidence than for $\phi = 80°$.

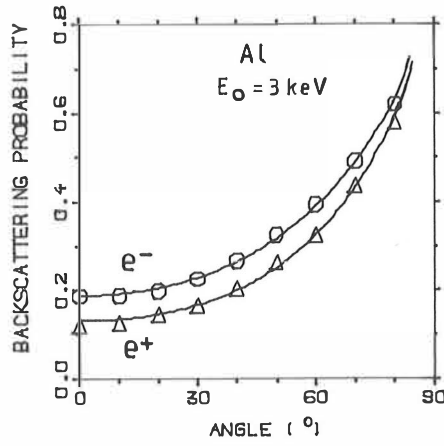

Fig. 18. Dependence of the backscattering probability on the angle of incidence for Al at 3 keV. The lines are fits of Eq. (20) to the MC points.

The backscattering probability $\eta_B(\phi)$ of positrons or electrons with the angle of incidence ϕ (with respect to the surface normal) can be presented as [Ka82]

$$\eta_B(\phi) = b\left(\frac{\eta_B(0)}{b}\right)^{\cos\phi}, \tag{20}$$

where $\eta_B(0)$ is the backscattering probability at normal incidence and b is an experimentally determined constant. Fits of Eq. (20) to the MC data for Al and W give $b = 0.80 \pm 0.02$ at 3 keV. Differences between positrons and electrons at each energy are smaller than the statistical uncertainty of MC simulations. b increases by ~ 0.02 for both particles when the incident energy is changed from 3 to 10 keV. Similar behaviour of backscattering as a function of entrance angle has

been found for 10–100 keV electrons [Ka82, Ni82]. At that energy region Kalef–Ezra *et al.* [Ka82] observed b to be 0.89, which agrees with the extrapolation of MC values. The reason for the increase of b with energy is that at high energies (above 10 keV) forward scattering becomes relatively more dominating.

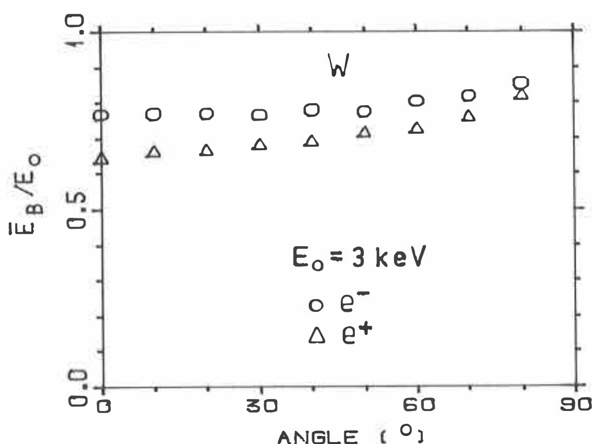

Fig. 19. The mean backscattering energy ($\overline{E}_B/E_0$) as a function of the incident angle for 3 keV electrons and positrons incident on semi–infinite tungsten.

Variation of the angle of incidence, ϕ, changes the backscattering energy distributions remarkably. The distribution does not change much in the range $\phi = 0° - 50°$. At more oblique angles of incidence the maximum shifts toward higher energies. Fig. 19 shows the increase of $\overline{E}_B$ as a function of incident angle for 3 keV projectiles incident on tungsten. The difference between positron and electron mean backscattering energy decreases as ϕ increases. For large ϕ the backscattering probability after a few collisions increases considerably and the projectile has less time to lose energy in inelastic collisions.

The Monte Carlo backscattering energy distributions of electrons are qualitati-

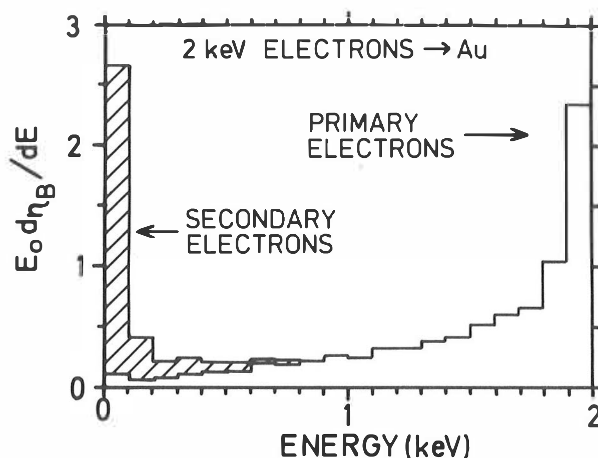

Fig. 20. Backscattering energy distributions of 2 keV primary and secondary electrons from semi-infinite gold. The termination energy of 10 eV is used.

vely similar to the experimental measured and theoretically extracted ones [Ic80, Sh83]. The contribution of energetic secondary electrons to the experimentally observed total backscattering is typically less than 10 % (Fig. 20 and [Ka82]) depending on the measuring geometry and the target material. The differences between experimental and MC electron backscattering coefficients (Figs. 11–14) can be explained by energetic secondary electrons.

The number of lobes in the differential elastic scattering cross section (Fig. 3) and their position depends on the material and energy of the incident electrons. They arise from the attractive potential of an atom for electrons, whereas the repulsive potential for positrons only causes the forward peak. Some conseque-nces of these large angle scattering lobes for electrons should be seen e.g. in the backscattering energy or angular distributions with good statistics and accuracy. On the contrary, in low energy electron diffraction (LEED), the effect of the peaks and zeros is most important, and complicates the multiple scattering calculation of

the LEED intensity curves. On the other hand, in low energy positron diffraction (LEPD) the analysis is much simpler due to the much smoother angular variation of the cross sections.

At energies around 1 keV the absorption probability of positrons in solid targets is around 85–90 %, which is much larger than was expected on the basis of the known electron absorption probabilities. The small backscattering probability of positrons at keV energies makes the use of low energy monoenergetic positron beams more effective. This is beneficial for the use of keV positrons as a probe to give information of the surface or near–surface region.

2.4. SLOWING DOWN IN SOLIDS

2.4.1. Implantation

The distribution of the trajectory endpoints in the material is cylindrical symmetric and deeper in the material resembles a half–sphere (Fig. 21). The distribution is qualitatively similar both for positrons and electrons. It only spreads out into smaller or larger volume depending on the incident energy of the projectile and the target material.

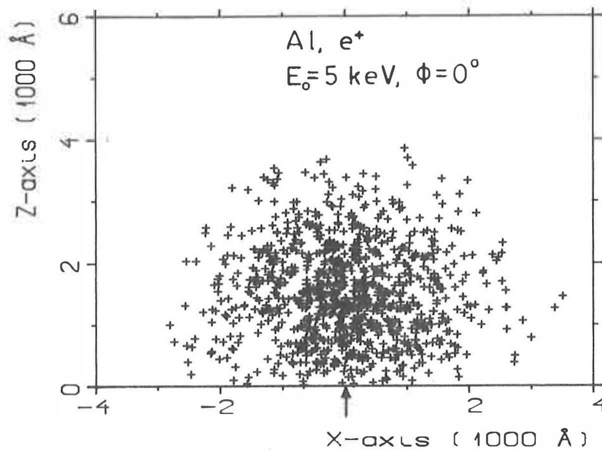

Fig. 21. Distribution of the trajectory endpoints, projected onto x–y plane, for 5 keV positrons at normal incidence on Al. The arrow denotes the entrance position.

Positrons go deeper into the material than electrons, which is seen in the mean penetration depths (Figs. 22–24). In heavy elements positrons penetrate up to 30 % deeper, whereas the difference in light elements is only a few percent. This result

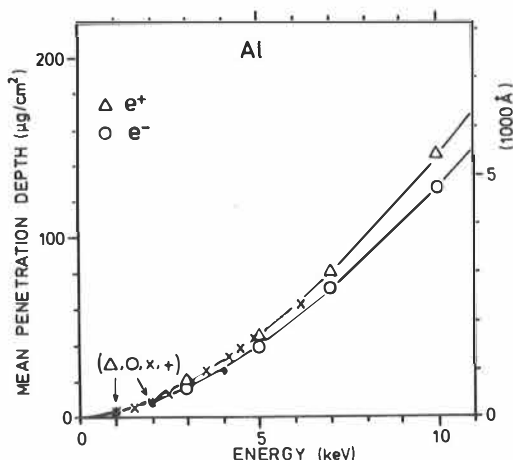

Fig. 22. Mean penetration depth vs. initial beam energy for semi-infinite Al. The crosses and pluses are experimental positron [Mi82b] and electron [Vy76] values, respectively. The lines are fits of Eq. (21) to the MC data.

agrees with earlier theoretical and experimental results for high energies [Ro54, Se55] and with qualitative expectations. The main reason is in the different elastic scattering cross sections of positrons and electrons (Figs. 3 and 4). Electrons have a distinctly larger probability to backscatter from atoms than positrons. This arises from the attractive force between electron and atom and from the lack of exchange effects between positron and core electrons. On the other hand, the indistinguishability of electrons increases the electron penetration depth by up to ~5 % and thus decreases the difference between electrons and positrons.

The mean penetration depth, $\bar{z}$, in a semi-infinite target can be described rather well by the formula

$$\bar{z} = \alpha E_0^n, \tag{21}$$

where E_0 is the incident energy and α and n are parameters, which are dependent

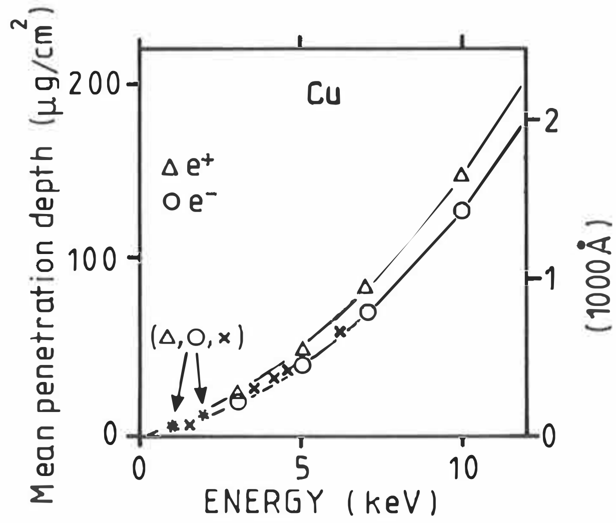

Fig. 23. Mean penetration depth vs. initial beam energy for semi-infinite Cu. The crosses are experimental positron values [Mi82b]. The lines are fits of Eq. (21) to the MC data.

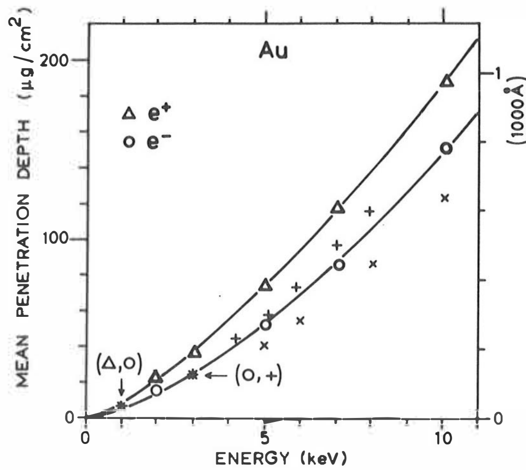

Fig. 24. Mean penetration depth vs. initial beam energy for semi-infinite Au. The crosses and pluses are experimental electron values of [Vy67] and [Ka59] , respectively. The lines are fits of Eq. (21) to the MC data.

Table 2. Parameters n and α for positron and electron mean penetration depths for N_2, Al, Cu, and Au. The statistical errors of calculated parameters in this and in further tables are typically the same or less than the accuracy of presentation.

Material	Positrons		Electrons	
	α [μg/cm^2]	n	α [μg/cm^2]	n
N_2	2.8	1.70	2.3	1.77
Al	3.2	1.66	2.7	1.67
Cu	4.2	1.55	3.1	1.62
Au	8.9	1.33	4.9	1.49

on the target material (Table 2). For electrons they are roughly $\alpha \simeq$ 2–5 μg/cm^2 and $n \simeq$ 1.5–1.8. For positrons, the dependence on target material is somewhat stronger (see Table 2 and Figs. 22–24). For both particles α increases and n slightly decreases as a function of atomic number. On the other hand, α and n correlate slightly and in lack of a more detailed knowledge reasonable values both for electrons and positrons in all materials are $\alpha = 4.0$ μg/cm^2 and $n = 1.6$.

Calculated mean penetration depths fit rather well with the experimental results. The experimental median positron penetration depths of Mills and Wilson [Mi82b] for Al and Cu are in agreement with MC mean values (Figs. 22 and 23). More experimental penetration depth data exist for electrons but, unfortunately, the scatter is large. However, on the average they agree well with the MC data (Figs. 22 and 24).

The simulated positron stopping profiles are compared with the experimentally deduced stopping profiles [Mi82b] for Al and Cu in Fig. 25. The maxima of the simulated distributions are higher than those of the experimental estimates and

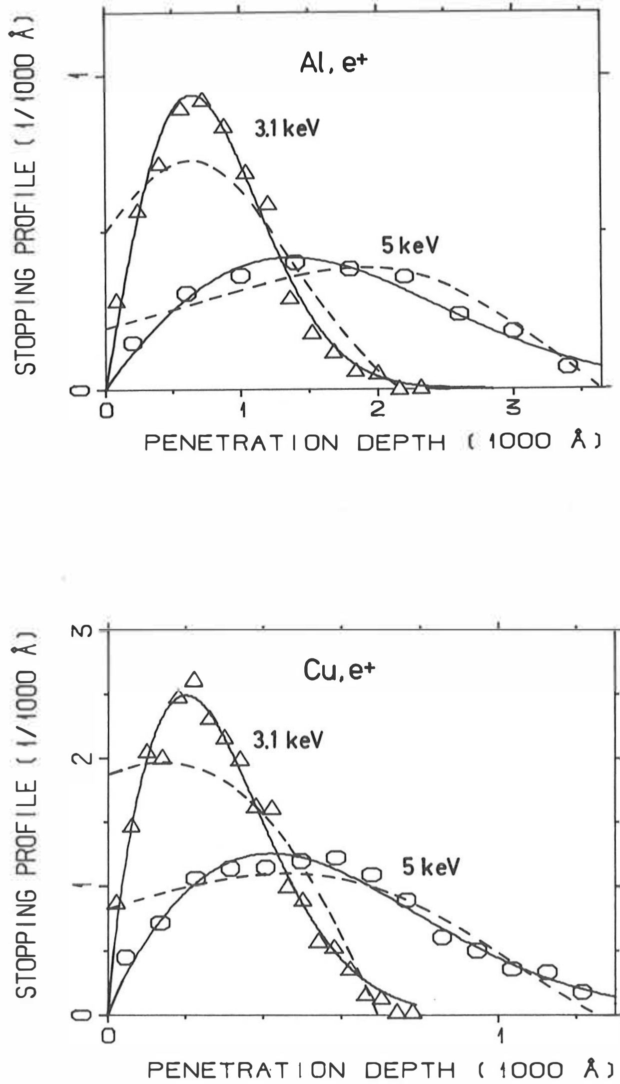

Fig. 25. Stopping profiles for 3.1 and 5 keV positrons in semi–infinite aluminum (above) and copper (below). The full curves denote the fits of Eq. (23) to the MC simulation data and the dotted lines the experimentally obtained derivatives of the positron transmission probability with respect to the film thickness ($-d\eta_T/dz_f$) [Mi82b]. (The curves have been normalized to have the same absorption probability for each incident energy, respectively).

the MC values near the surface are lower, respectively. These differences arise from ignoring the increase of the backscattering probability as a function of film thickness in the experimental analysis, which is important especially for thin films. If the backscattering effect is taken into account, the experimental curves would be much lower near the surface and thereby the maximum values would increase due to normalization.

The experimental positron stopping profiles are also slightly higher deep in the material than the MC profiles. In thin film experiments positrons cannot return back to the material after transmission, whereas in the bulk the backscattering from deep layers nearer to the surface is considerable. This explains the differences between MC and experimental profiles deep in the material. Taken all together, the agreement between MC and experimental stopping profiles is good. Difficulties in estimating positron and electron implantation profiles from thin film transmission measurements are discussed in more detail in the next chapter.

Resently Vehanen *et al.* [Ve87] have experimentally confirmed that the shape of the positron implantation profile possesses a derivative of a Gaussian function (Eq. (23)), in contrast to the more commonly used exponential profile. They measured the annihilation line–shape parameter [Ha79] as a function of positron implantation energy in multilayer structures of Al_2O_3, Al_2O_3/ZnS, or $Al_2O_3/ZnS/Al_2O_3$ grown on a glass substrate. The mobility of thermalized positrons was observed to be very low in these materials and the authors were indeed detecting the situation just after implantation. Furthermore, the annihilation line–shape parameter has a distinct value in each of the studied material, and therefore the measurements were very sensitive to the shape of the positron implantation profile. The use of Gaussian implantation profiles (Eq. (23)), with parameter values of $m = 2.0 \pm 0.1$, $\alpha = 4.0 \pm 0.3$ $\mu g/cm^2$, $\alpha_0 = 4.5 \pm 0.4$ $\mu g/cm^2$, and $n = 1.62 \pm 0.05$, reproduced the experimental annihilation line–shape parameter vs. E_0 curvers very nicely, whereas the exponential function failed totally. The simulated parameter values for Al

and Cu (see Tables 2 and 4) are in reasonable agreement with the experimentally deduced ones.

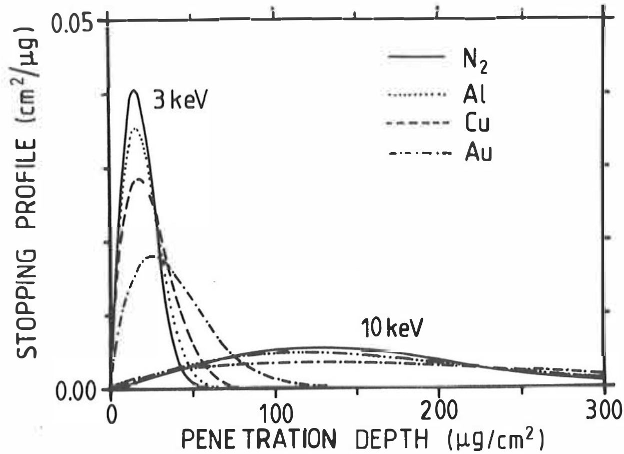

Fig. 26. Fits of Eq. (23) to the stopping profiles (normalized to unit area) of 3 and 10 keV positrons in semi–infinite N_2, Al, Cu, and Au, with the penetration in units of $\mu g/cm^2$.

Positron stopping profiles for four representative materials considered in this work are given in Fig. 26 for two energies. The distributions are quite similar over a wide range of elements, and the formula (23) describes the stopping profile well for all elements. The small increase of the penetration depth, in units of g/cm^2, with atomic number of the target material can also be seen. The increase of the penetration depth as a function of atomic number is smaller for electrons than for positrons.

The distribution of the trajectory endpoints for 5 keV positrons at incident angle of 80° impinging on Al is shown in Fig. 27. The distribution is almost similar to the one for normal incidence (Fig. 21), which implies that only small changes take place in the shape of the stopping profile and in the mean penetration

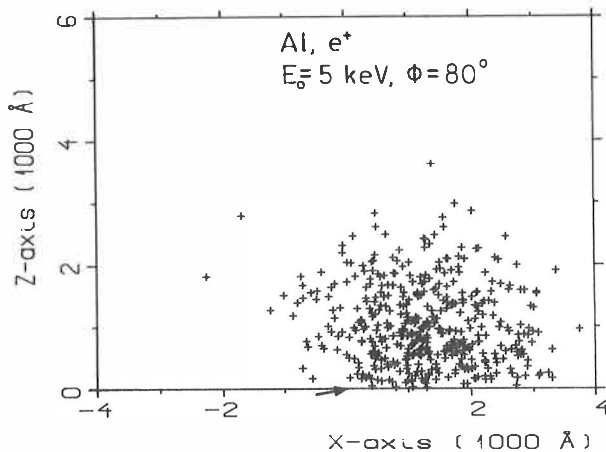

Fig. 27. Distribution of the trajectory endpoints, projected onto x–y plane, for 5 keV positrons at 80° angle of incidence on Al. The arrow denotes the entrance position.

depth at oblique incident angles. The reason for similar shapes of the trajectory endpoints for different incident angles is that the projectiles lose the knowledge of their initial direction after a few collisions.

Between 0° (normal incidence) and 30°, the change of the incident angle does not have much effect on the penetration properties (Figs. 28 and 29). With larger angles do the results start to differ from those of normal incidence. The decrease of the mean penetration depth is 20 % – 30 % for 3 keV projectiles incident on Al and W when the incident angle is changed from 0° to 80°. It is a little smaller for electrons than for positrons. The decrease of the penetration depth naturally shifts the implantation profiles closer to the entrance surface (Fig. 29). The differences in penetration depth between 0° and 80° decrease with energy. They are also smaller for heavy materials (W) than for light materials (Al). The reason is that projectiles have larger probability to scatter elastically into large angles

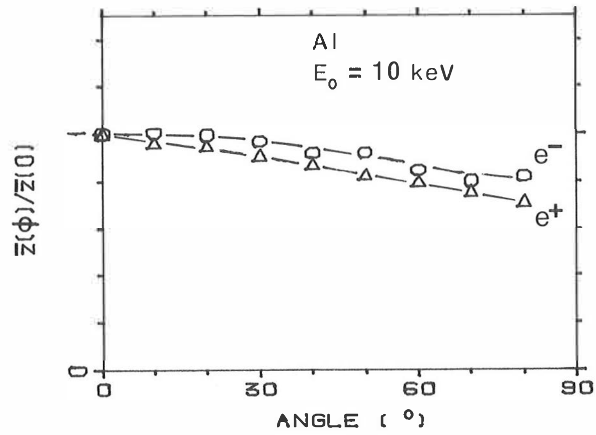

Fig. 28. Mean penetration depth as a function of incident angle for 10 keV projectiles impinging on Al. The lines are drawn just to guide the eye.

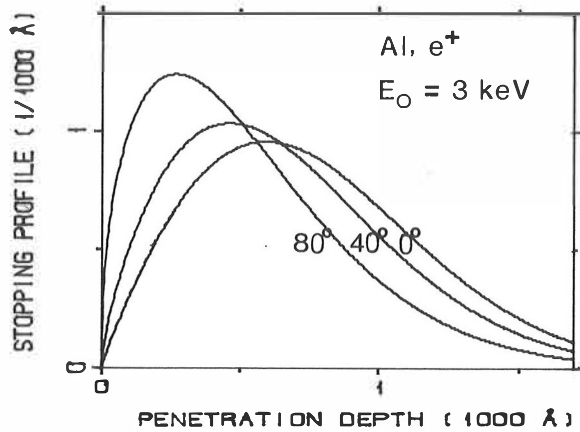

Fig. 29. Fits of Eq. (23) to the stopping profiles (normalized to unit area) of 3 keV positrons on Al for 0°, 40°, and 80° incident angles.

from heavy atoms than from light atoms. Therefore projectiles lose the knowledge of their original direction faster in heavy materials than in light ones.

2.4.2. Energy deposition

Energetic positrons and electrons lose their energy in the material mainly in ionization and excitation processes. Only at low energies, where the MC simulation is cut off, phonon excitations and other temperature dependent phenomena become important. The ionization distributions as a function of the penetration depth are quite similar for all electron levels. Of course, the ionization profiles of the most tightly bound electron levels are somewhat closer to the surface than the profiles for less bound electron levels. The reason is that projectiles have lost their energy in penetrating into the material and the remaining energy is not sufficient to ionize the most tightly bound electrons deep in the material, but is enough to ionize the less bound electrons.

The ionization and energy deposition profiles are also similar, because the ionization profiles of different electron levels are alike. This is especially true for the ionization profile of the least bound electrons, because collisions with them dominate during the slowing down of projectiles. The agreement between the energy deposition profile and the ionization profile of the least bound electrons is best for light elements, but is still rather good for heavy elements (Fig. 30). This result is significant for the experimental energy deposition profile determinations. It supports the commonly used assumption that the ionization profile of the least bound electrons (or the excitation profile of a low energy excitation state) is equal to the energy deposition profile. All the analysis for the energy deposition and ionization profiles gave practically equal results. Therefore only the energy deposition profiles are discussed here in more detail.

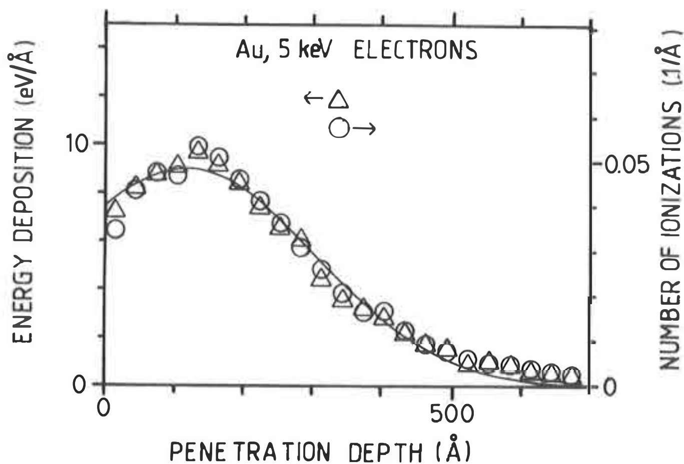

Fig. 30. The energy deposition profile and the ionization profile of the least bound electrons as a function of the penetration depth for 5 keV electrons incident on Au. The profiles have been scaled to have the same area. The solid line is a Gaussian fit (Eq. (33)) to the energy deposition profile.

The energy deposition profiles have been determined experimentally mainly for small atomic number gases. For small atomic numbers the energy deposition distributions can be presented by a uniform distribution [Gr57], where the penetration depth is given in units of the mean penetration depth (or the experimentally deduced practical range) and the energy deposition is given in units of the stopping power. In Fig. 31 the simulated energy deposition profile for N_2 is compared to experimental and theoretical profiles for air and good agreement is found, in particular with the experimental data of Grün [Gr57]. The agreement is also good with experimental profiles of Barrett and Hays [Ba76] for 1 and 3 keV electrons incident on N_2.

The mean energy deposition depth, $\overline{z}_E$, behaves similarily as a function of incident energy to the mean penetration depth (Eq. (21)). The MC parameters

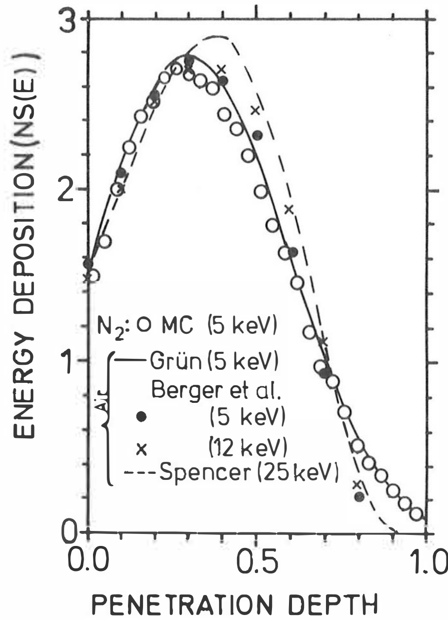

Fig. 31. Energy deposition distribution of 5 keV electrons in semi-infinite solid N_2 and air along the surface normal. The energy deposition is plotted in units of the stopping power $N \times S(E)$ and the depth in units of the maximum penetration depth [Be70]. Monte Carlo distribution for 5 keV electrons in N_2 is plotted to have the same surface density unit (g/cm^2) as the experimental distribution of Grün [Gr57] for 5 keV electrons in air. The dashed line is a theoretical curve of Spencer [Sp59] and the crosses and circles are from Monte Carlo calculations of Berger *et al.* [Be70] for air.

of equation $\bar{z}_E = \alpha_E E_0^n$ for positron and electron mean energy deposition depths are shown in Table 3. The energy deposition profiles are somewhat closer to the surface than the stopping profiles and therefore the values of α_E for the mean energy deposition depth are also a little smaller than those of α for the mean penetration depth (Table 2). But the n–values are almost equal, because the behaviour as a function of energy is similar.

Table 3. Parameters n and α_E for positron and electron mean energy deposition depths for N_2, Al, Cu, and Au.

Material	Positrons		Electrons	
	α_E [μg/cm^2]	n	α_E [μg/cm^2]	n
N_2	1.9	1.77	2.2	1.70
Al	2.1	1.69	2.5	1.67
Cu	3.2	1.55	2.4	1.63
Au	6.7	1.35	3.8	1.49

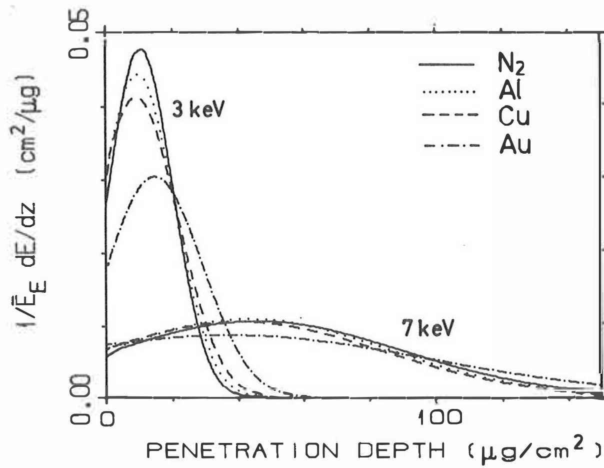

Fig. 32. Fits of Eq. (33) to the energy deposition profile as a function of the penetration depth for 3 and 7 keV electrons incident on N_2, Al, Cu, and Au. The mean deposited energies, $\overline{E}_E$, are presented in Table 5.

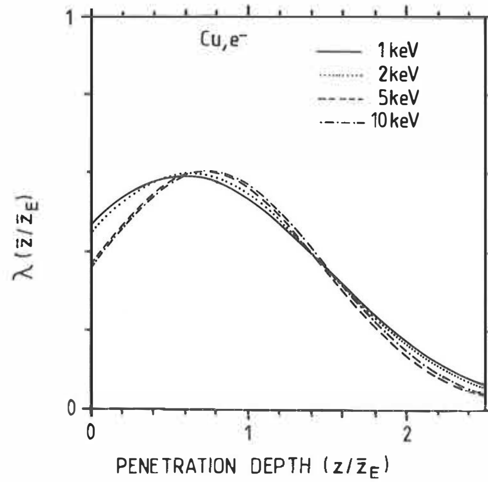

Fig. 33. Fits of Eqs. (33) and (34) to the energy deposition profile as a function of the penetration depth for 1, 2, 5, and 10 keV electrons incident on Cu.

From the parameter values of Table 3 can be seen that the mean energy deposition depths in surface density units are of the same order of magnitude for all elements. The mean energy deposition depth increases a little with atomic number, but the distribution has the Gaussian shape for all elements (Fig. 32). The energy deposition distributions can be presented by a uniform distribution $\lambda(z/\bar{z}_E)$ (see the next chapter), where the penetration depth unit is $\bar{z}_E$ and the distributions are normalized to unit area. This scaling would move all the curves in Fig. 32 almost on top of each other. This is seen for the energy deposition curves of 1, 2, 5, and 10 keV electrons incident on Cu in Fig. 33.

The energy deposition (and implantation) distributions and their mean depths are quite similar in all elements and for both projectiles. Nevertheless the slowing down process is different in light elements from the one in heavy elements. In light elements, such as hydrogen, the elastic scattering takes place only to very small angles and the projectiles slow down along their path near the initial direction.

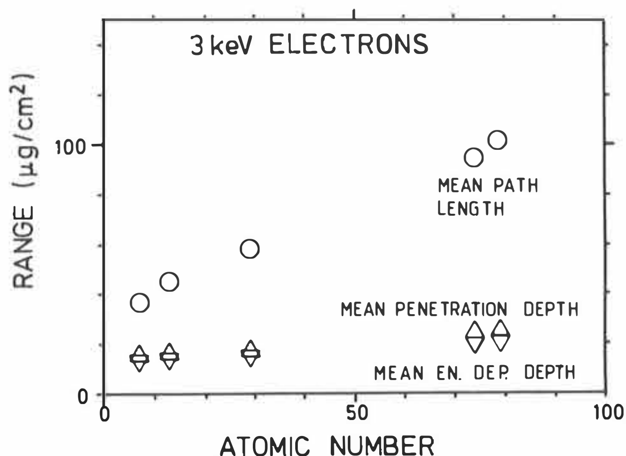

Fig. 34. Mean path length, mean penetration depth, and mean energy deposition depth as a function of atomic number for 3 keV electrons.

For the lightest elements the mean total path length is only a little longer than the mean penetration depth. For materials of large atomic number the mean total path length is several times longer than the mean penetration depth (Fig. 34). The projectiles wander a long way in heavy materials before they have slowed down, but they lose the knowledge of their initial direction after a couple of collisions and the movement resembles qualitatively a random walk.

2.5. PARAMETRIZATION OF THE IMPLANTATION AND ENERGY DEPOSITION PROFILES

2.5.1. Implantation Profile

In order to obtain some useful parameters for implantation profiles the ideas of Makhov [Ma60] and those later applied by Hansen and Ingerslev–Jensen [Ha83] have been used. The approximate transmission curve of Makhov is

$$\eta_T(z) \simeq \exp\left[-\left(\frac{z}{z_0}\right)^m\right], \tag{22}$$

where m=$m(Z,E)$ is found to be a decreasing function of atomic number Z [Vy73b, Ha83] and an increasing function of incident electron energy E_0 [Vy73a, Vy73b, Fi74, Vy76]. Accordingly the approximate formula for the stopping profile is

$$P(z) = \frac{mz^{m-1}}{z_0^m} \exp\left[-\left(\frac{z}{z_0}\right)^m\right], \tag{23}$$

i.e. the negative of the derivative of Eq. (22). Eq. (23) has been fitted to the Monte Carlo stopping profiles in semi–infinite N_2, Al, Cu, and Au. A common feature is that the MC stopping profiles can be described very well by a function of just two parameters. In fact the shape parameter m is nearly constant ($\sim$ 1.9) in the energy range 1–10 keV (Fig. 35) and Eq. (23) reduces to be only a function of z_0 for all the four materials investigated here. The value of m for positrons is a little larger (by $\sim$0.1) than that of electrons.

Experimental values for the parameter m for electrons have been established by many authors. In aluminum the values of m have been found to be between 1.7 and 2.0 [Ma60, Vy73a, Vy73b, Vy76, Fi74] and in copper close to 1.65 [Ma60, Vy67, Vy73a, Fi74, Vy77]. For both materials the values of m are slightly smaller than

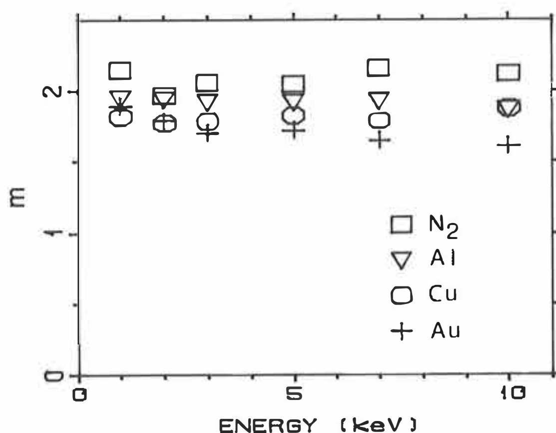

Fig. 35. Parameter m as a function of the incident energy for positrons incident on N_2, Al, Cu, and Au.

the theoretical results of this work (Fig. 35). In gold there is a clear disagreement between the Monte Carlo and experimental results. The experimentally extracted m value is 1.25 [Vy67, Vy77] and the Monte Carlo calculation gives 1.75.

The reason for this disagreement seems to be that experimenters have fitted Eq. (22) to thin film transmission distributions, in which the backscattering effect has not been taken into account, whereas in this work Eq. (23) has been fitted to the Monte Carlo stopping profiles in bulk. Backscattering has a strong influence on the transmission probability vs. gold film thickness distributions (a large backscattering coefficient), but less on those in copper and aluminum. Thus the change of backscattering fraction as a function of film thickness might explain the difference. Although Vyatskin and Khramov [Vy76], and Vyatskin *et al.* [Vy77] claim that their measurements have been made in bulk geometry, so that given transmission probabilities should correspond to penetration probabilities in bulk, they have obtained same m values as previously in film transmission measurements. This seems to imply a discrepancy, because differentiation of the film transmission

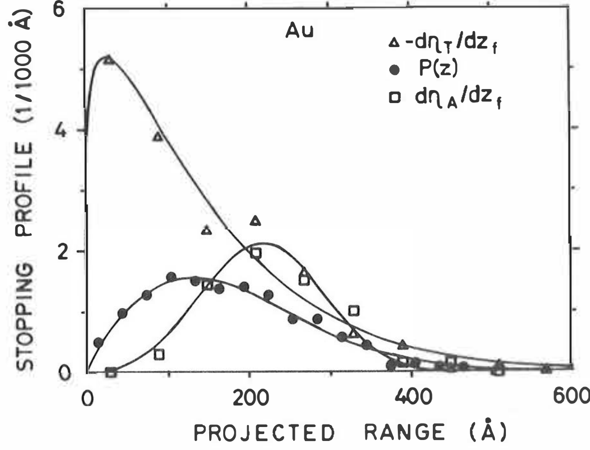

Fig. 36. Penetration depth distribution of 5 keV electron incident on Au [Va83]. η_T and η_A are the transmission and absorption probabilities, respectively, z_f is the film thickness, and $P(z)$ is the stopping profile in semi-infinite Au. Solid lines are fits of Eq. (23) to the MC distributions.

curve gives a stopping profile different from the real one.

To verify this assumption 5 keV electron transmission calculations through gold films were performed [Va83] for thicknesses of 30 Å intervals. The calculated stopping profile from the transmission distribution $-d\eta_T/dz_f$, from the film absorption distribution $d\eta_A/dz_f$, and the real distribution $P(z)$ in bulk are shown in Fig. 36. Fits of Eq. (23) to $-d\eta_T/dz_f$, $P(z)$ and $d\eta_A/dz_f$ gave m values 1.15, 1.83 and 3.38, respectively. This result shows clearly the differences between the real stopping profile and the other two. The m value from $-d\eta_T/dz_f$ is of the same order of magnitude than the experimental values. $-d\eta_T/dz_f$ overestimates the stopping probability in a semi-infinite target near the surface. $d\eta_A/dz_f$ on the contrary underestimates the stopping profile near the surface and overestimates it deep in the material. The backscattering effect explains also the small differences between the experimental and the Monte Carlo m-values in Al and Cu.

Table 4. Parameters α_0, n, and m (for 5 keV) in the fits of Eqs. (23) and (25) to the MC data of positrons incident on N_2, Al, Cu, and Au. m values for other positron energies are shown in Fig. 35. The statistical accuracy of m is ± 0.05.

Material	α_0 [μg/cm^2]	n	m
N_2	3.3	1.71	2.05
Al	3.7	1.67	1.92
Cu	5.0	1.54	1.83
Au	10.6	1.32	1.72

The mean penetration depth $\bar{z}$ can be written in terms of z_0 as

$$\bar{z} = \Gamma(1 + 1/m) z_0, \tag{24}$$

where $\Gamma(x)$ is the gamma function. For m–values calculated from the MC stopping profiles Eq. (24) gives $z_0 \approx 1.13\bar{z}$. This can be used as an approximation for z_0 if $\bar{z}$ is known. z_0, of course, behaves similarily as a function of incident energy as $\bar{z}$ and can be written as

$$z_0 = \alpha_0 E_0^n, \tag{25}$$

where α_0 is roughly 1.13α and n is practically the same as for $\bar{z}$. These three parameters α_0, n, and m (Table 4 and Fig. 35) are able to fully describe positron implantation profiles for example for analysis of slow monoenergetic positron beam experiments.

2.5.2. Re–emission of Positrons

In experiments with slow positron beams [Mi82a] a key quantity of interest is the re–emission yield of positrons (or positronium atoms) from the entrance surface. There are various physical phenomena associated with this yield, but underlying all is the diffusion of the implanted and thermalized positrons to the surface. It has been shown [Ni80] that the overall re–emission probability is

$$F = \nu \left[\frac{1}{(\lambda D)^{1/2}} - \frac{\nu}{\nu(\lambda D)^{1/2} + \lambda D} \right] \times I, \tag{26}$$

where

$$I = \int_0^\infty dz P(z) \exp\left[-\left(\frac{\lambda}{D}\right)^{1/2} z \right]. \tag{27}$$

Above, D is the diffusion constant, λ the depletion (disappearance) rate of free positrons in the medium, and ν the rate of emission from the surface. $P(z)$ is the implantation profile (normalized to unit area).

Using the calculated profiles fitted to the analytic form of Eq. (23), the re–emission parameters, I, have been obtained, which are the Laplace transforms of the stopping profile for different values of the Laplace variable $s = (\lambda/D)^{1/2}$. These results are displayed in Figs. 37–39, which should be useful in a quantitative analysis of slow positron beam experiments. In Fig. 37 the parameter I for aluminum is shown as a function of incident energy, E_0, for a value of the Laplace parameter $s = 0.001$ Å^{-1}. The results based on the MC calculations (m=2) are compared with the formula obtained by substituting Eq. (23) with m=1 into Eq. (27),

$$I = \frac{1}{1 + z_0 s}. \tag{28}$$

This approximation is valid only for the exponential stopping profile. It and the formula commonly used to fit experimental data (see e.g. [Mi82a]) are identical provided that the value of the incident energy at which the re–emission has degraded to half its maximum (useally denoted by E_0) is equal to $(1/s\alpha_0)^{1/n}$. The

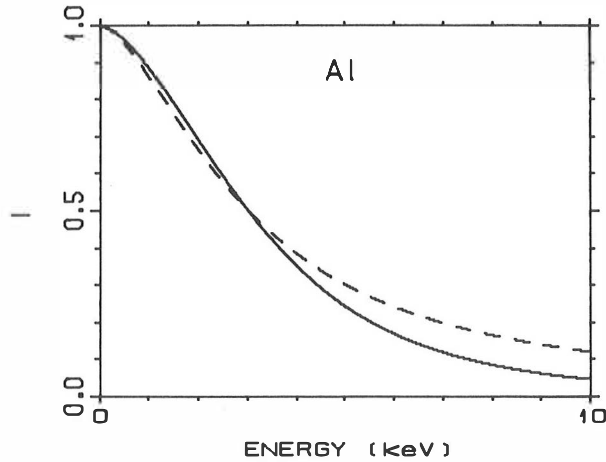

Fig. 37. Positron re-emission parameter I vs. the incident energy E_0 for aluminum. The solid line is calculated using (27) and the MC data and the dotted curve is the estimate of (28) with the half-width energy of 3.02 keV (s = 0.001 Å^{-1}, α_0 − 137 Å and n = 1.67).

approximation (28) is qualitatively correct but can lead to errors in quantitative analysis. For example, using the Al depletion rate $\lambda = 6.02 \times 10^9$ s^{-1} [Fl78], the full curve in Fig. 37 corresponds to the diffusion constant D = 0.60 cm^2/s. If one on the other hand uses Eq. (28) and just takes the half-width energy of 3.02 keV from Fig. 37, Eq. (28) leads to D = 0.45 cm^2/s. A similar effect has been observed in analysing experimental positronium fraction at silicon surfaces vs. incident positron energy data [Ni85]. The experimental data is described well by the Makhov-type implantion profile (Eq. (23) with m=2.0). One should also note that at small energies diffusion back to the surface is not sensitive to the shape of the implantation profile whereas at high energies the type of the profile is crucial. The conclusion is that for accurate analysis the nomograms of Figs. 38 and 39 are to be preferred.

When the stopping profile formula (23) is substituted into Eq. (27) and one

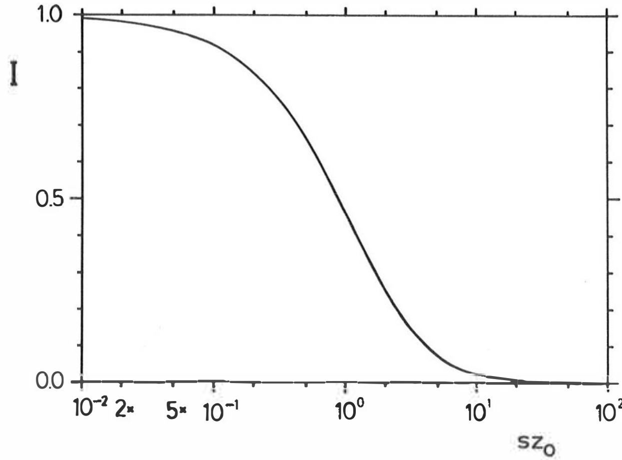

Fig. 38. Positron re–emission parameter I vs. the product of the diffusion parameter s and the penetration depth parameter z_0.

denotes $x = z/z_0$, the re–emission parameter can be written as

$$I = \int_0^\infty dx \; m \; x^{m-1} exp\{-x^m - sz_0 x\} \,. \tag{29}$$

The positron re–emission parameter I depends only on the product of the diffusion parameter s and the penetration parameter z_0, because the parameter m is almost independent of material. If the diffusion parameter s is known and z_0 can be calculated from Eq. (25), the positron re–emission parameter can be determined from Fig. 38.

The re–emission parameter I as a function of the parameter m is show in Fig. 39 for different values of the product sz_0. I changes appreciably only at small m values ($m \leq 1.5$), where the stopping profile resembles more an exponential profile. The re–emission parameter I does not depend much on m in the range of m–values corresponding to the MC–simulations for positrons ($m \approx 2.0$).

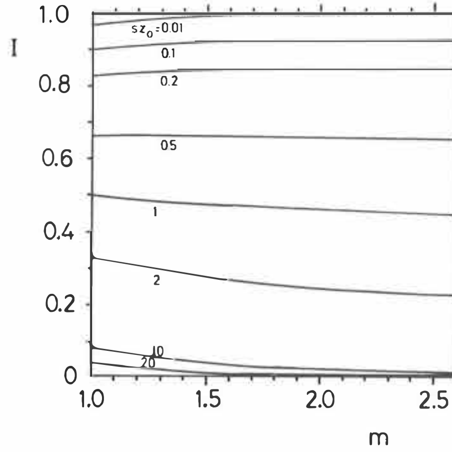

Fig. 39. Positron re-emission parameter I vs. the stopping profile parameter m for different values of sz_0.

When $m = 2.0$, Eq. (29) can be writen as

$$I = 1 - \frac{\sqrt{\pi}}{2} sz_0 \exp\left[\left(\frac{sz_0}{2}\right)^2\right] \operatorname{erfc}\left(\frac{sz_0}{2}\right), \tag{30}$$

where

$$\operatorname{ercf}(x) = \frac{2}{\sqrt{\pi}} \int_x^{\infty} \exp(-t^2) dt. \tag{31}$$

This is in practice an accurate expression for the positron re–emission parameter, because I depends very little on m (Fig. 39). Eq. (30) can be expressed also as a power series

$$I = 1 - \sqrt{\pi} \sum_{n=0}^{\infty} \frac{1}{n!} \left[\frac{sz_0}{2}\right]^{2n+1} + \sum_{n=0}^{\infty} \left\{ \sum_{k=0}^{n} \frac{2(-1)^k}{(n-k)!k!(2k+1)} \right\} \left[\frac{sz_0}{2}\right]^{2(n+1)}, \tag{32}$$

which converges with increasing n.

Changing the angle of incidence, θ, has an effect on the shape of the stopping profile (Fig. 29). This is also seen as a decrease of m with increasing angle of incidence. Positrons have larger values of m than electrons at small angles, but

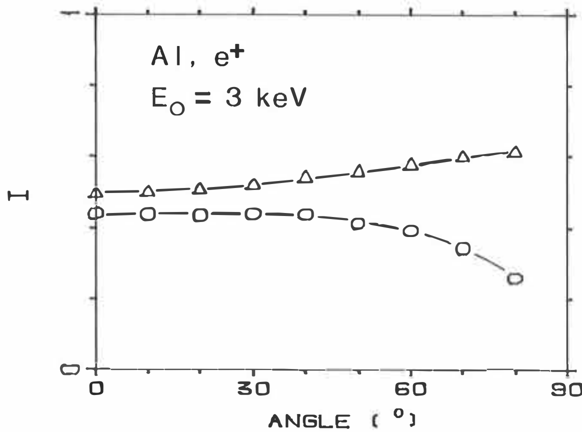

Fig. 40. Re–emission parameter I as a function of the incident angle for 1 keV positrons on Al. Triangles denote I values with $P(z)$ normalized to unit area and circles are the same multiplied by the absorption probability ($s = 0.001$ Å^{-1}).

the m value decreases more rapidly for positrons than for electrons with increasing angle. The decrease of m as a function of incident angle is almost the same for all energies. For example, when the angle of incidence on Al changes from 0° to 80°, m decreases from 1.91 (±0.03, typically) to 1.49 and from 1.84 to 1.60 for 3 keV positrons and electrons, respectively. The decrease for 10 keV positrons and electrons is from 1.87 to 1.53 and from 1.87 to 1.55, respectively.

The positron re–emission parameter, I, does not change much below the incident angle of 30°. At larger angles the decrease of the mean penetration depth with θ increases I, if $P(z)$ is normalized to unit area. If, however, the increase of backscattering as a function of θ is taken into account, the re–emission probability will decrease as a function of the incident angle. The behaviour of the re–emission parameter I as a function of the incident angle is show in Fig. 40 for 3 keV positrons incident on Al.

2.5.3. Energy Deposition Profile

To parametrize electron and positron energy deposition profiles maybe the most practical units would be the projected range for length and the stopping power for energy deposition. Actually, these units work well for light materials and almost a universal profile is obtained. However, the increase of the backscattering probability as a function of atomic number prevents the stopping power to scale the energy deposition profiles in all materials to a universal curve. Grün [Gr57] has presented a more universal parametrization by normalizing the distributions to unit area and it is presented here.

A prerequisite for the universal parametrization is that all energy deposition profiles observe a similar shape, as a Gaussian formula in the present case. The Gaussian distribution for the energy deposition profiles can be written as

$$D(z) = n'\overline{E}_E \left(2\pi\sigma_D^2\right)^{-1/2} \exp\left[\frac{-(z-r_D)^2}{2\sigma_D^2}\right], \tag{33}$$

where n' is a unitless scaling factor, $\overline{E}_E$ is the mean deposited energy per incident particle in the material, r_D is the mean range of the formula, and σ_D the standard deviation. A fit of Eq. (33) to the energy deposition profile of 5 keV electrons in Au is shown in Fig. 30 and good agreement is observed. The agreement for Au is actually worst for all the simulated materials, because Au is the heaviest one. The energy deposition profiles follow the Gaussian profile better for light elements than for heavy elements.

Following the ideas of Grün [Gr57] a universal parametrization for the energy deposition profile can be written as

$$D(z) = \frac{E_E}{\overline{z}_E}\,\lambda\left(\frac{z}{\overline{z}_E}\right), \tag{34}$$

where $\overline{z}_E$ is the mean energy deposition depth and $\lambda(z/\overline{z}_E)$ is a unitless function of a unitless depth parameter $z/\overline{z}_E$. The energy deposition distributions $\lambda(z/\overline{z}_E)$

for 1, 2, 5, and 10 keV electrons in Cu are shown in Fig. 33. The profiles $\lambda(z/\overline{z}_E)$ are quite similar through the studied energy range as well as for all the studied materials. The Gaussian parameters for electrons and positrons incident on N_2, Al, Cu, and Au are presented in Tables 5 and 6, respectively, for different incident energies.

However, it must be pointed out that $\lambda(z/\overline{z}_E)$ is the same only within a certain energy region, which moves toward higher energies with increasing atomic number of the target material. For example, the energy deposition profile of 1 keV electrons incident on Au includes only the decreasing part of the Gaussian distribution and deviates clearly from the profiles presented in Figs. 30–33. On the other hand, for incident particle energies inside a valid region the energy deposition profile can be calculated from Eq. (34), since the ratio E_E/E_0 is in practice a material constant (Tables 5 and 6), $\overline{z}_E = \alpha_E E_0^n$, and $\lambda(z/\overline{z}_E)$ is known.

Table 5. Parameters of the Gaussian fits to the energy deposition profiles of electrons incident on N_2, Al, Cu, and Au for different initial energies E_0. E_E is the mean energy deposited by an incident electron, $\bar{z}_E$ the mean energy deposition depth, n' a scaling factor of the Gaussian distribution, r_D the mean range of the Gaussian profile, and σ_D the standart deviation.

Material	E_0 [keV]	E_E [keV]	z_E [μg/cm^2]	n'	r_D [μg/cm^2]	σ_D [μg/cm^2]
N_2	1	0.925	2.10	1.03	1.50	1.71
	2	1.860	6.67	1.23	5.14	5.13
	3	2.830	13.05	1.18	10.43	9.64
	5	4.677	31.69	1.16	25.76	23.36
	7	6.558	57.15	1.16	44.97	44.59
	10	9.422	108.16	1.19	90.37	78.71
Al	1	0.868	2.46	1.27	1.56	2.09
	2	1.750	7.13	1.24	4.86	5.83
	3	2.633	13.61	1.23	9.53	11.01
	5	4.405	31.81	1.22	22.74	25.67
	7	6.163	56.62	1.17	42.58	42.87
	10	8.851	103.76	1.21	76.47	82.38
Cu	1	0.792	2.94	1.62	1.12	3.21
	2	1.622	8.15	1.27	5.23	6.90
	3	2.425	14.45	1.29	9.13	12.44
	5	3.959	32.88	1.11	23.98	24.26
	7	5.421	55.73	1.16	39.88	43.83
	10	7.871	101.52	1.12	76.12	75.35
Au	1	0.737	5.31	3.64	-5.29	9.45
	2	1.375	12.37	1.81	1.77	15.44
	3	1.970	19.98	1.09	14.60	14.26
	5	3.228	41.28	1.32	22.60	35.92
	7	4.475	68.82	1.35	36.04	61.67
	10	6.277	119.08	1.32	63.74	103.27

Table 6. Parameters of the Gaussian fits to the energy deposition profiles of positrons incident on N_2, Al, Cu, and Au for different initial energies E_0. $\overline{E}_E$ is the mean energy deposited by an incident electron, $\overline{z}_E$ the mean energy deposition depth, n' a scaling factor of the Gaussian distribution, r_D the mean range of the Gaussian profile, and σ_D the standart deviation.

Material	E_0 [keV]	$\overline{E}_E$ [keV]	$\overline{z}_E$ [μg/cm^2]	n'	r_D [μg/cm^2]	σ_D [μg/cm^2]
N_2	1	0.958	2.46	1.17	1.95	1.85
	2	1.925	7.33	1.19	5.60	5.67
	3	2.875	14.44	1.17	11.43	10.90
	5	4.794	34.19	1.14	28.01	24.55
	7	6.710	60.39	1.15	50.13	43.76
	10	9.557	110.87	1.15	91.68	80.76
Al	1	0.941	3.10	1.23	2.19	2.53
	2	1.866	8.45	1.22	6.15	6.77
	3	2.785	15.82	1.21	11.65	12.51
	5	4.538	35.83	1.22	26.39	29.08
	7	6.348	63.37	1.21	47.19	50.25
	10	9.097	115.96	1.22	85.45	93.58
Cu	1	0.927	3.88	1.32	2.38	3.45
	2	1.799	10.31	1.10	7.94	7.48
	3	2.639	18.57	1.29	11.98	16.23
	5	4.310	39.42	1.13	30.68	29.49
	7	5.795	65.05	1.17	49.69	51.19
	10	8.356	116.84	1.14	91.70	87.93
Au	1	0.912	7.26	1.28	4.62	6.17
	2	1.754	17.49	1.29	10.85	15.09
	3	2.498	29.34	1.16	20.95	23.19
	5	4.129	58.29	1.17	42.39	46.45
	7	5.507	93.03	1.16	65.35	73.45
	10	7.522	149.57	1.14	103.60	114.22

3. MOLECULAR DYNAMICS SIMULATIONS OF NEAR–SURFACE PHENOMENA

3.1. MOLECULAR DYNAMICS SIMULATION METHOD

In a molecular dynamics computer simulation the essential task is to solve numerically Newtonian equations of motion for atoms with properly defined mutual interactions. Numerically the equations are effectively solved by using the third order predictor–corrector –method [Be76] combined from the procedures of Rahman [Ra64] and Verlet [Ve67]. Knowing the position $\bar{r}_i$ and velocity $\bar{v}_i$ of the ith atom at time t and the acceleration $\bar{a}_i$ at time $t - \Delta t$ and t the new particle position after timestep Δt can be calculated from the algorithm

$$\bar{r}_i(t + \Delta t) = \bar{r}_i(t) + \Delta t\, \bar{v}_i(t) + \left(\frac{\Delta t^2}{6}\right) \{4\, \bar{a}_i(t) - \bar{a}_i(t - \Delta t)\}. \tag{35}$$

The acceleration of the ith atom in an N atom system is given by the Newton's equation

$$\bar{a}_i(t) = -\frac{1}{m_i} \sum_{j=1, j\neq i}^{N} \nabla_i V(r_{ij}(t)), \tag{36}$$

where m_i is the mass of particle i, $V(r_{ij}(t))$ is a pair potential, and $r_{ij}(t) = |\bar{r}_i(t) - \bar{r}_j(t)|$. Calculating the acceleration at time $t + \Delta t$ by Eqs. (35) and (36) the velocity at time $t + \Delta t$ can be calculated by

$$\bar{v}_i(t + \Delta t) = \bar{v}_i(t) + \left(\frac{\Delta t}{6}\right) \{2\, \bar{a}_i(t + \Delta t) + 5\, \bar{a}_i(t) - \bar{a}_i(t - \Delta t)\}. \tag{37}$$

Now all the necessary parameters are known for the timestep $t + \Delta t$ and one can return to (35) and proceed in calculating them for $t + 2\Delta t$. By repeating this procedure the atomic paths in a material can be followed.

Molecular dynamics simulation is a very powerful method for materials research, but it has also limitations. From physical point of view it is often limited by the lack of accurate interatomic potentials. The knowledge of the interactions between particles is crucial for many simulations. On the other hand, the computer resources give the upper limit for the number of particles N in the computational unit cell and for the time period of the simulated processes. The practical upper limit for N is a few ten thousand particles and for the duration of the simulated process around a nanosecond in real time. These numbers translate to several CPU hours on large computers. The discrete timestep Δt, which must be a small fraction of the vibration time of atoms in solid structure, restricts the time scale.

In the following the applied interactions between atoms and the simulation procedures of sputtering and surface melting are described. Simulation of damage production during sputtering of Al (110) surface by energetic Ar^+ ions is described in chapter 3.1.1. Chapter 3.1.2. includes the details of the simulation of melting of Lennard–Jones (111) surfaces.

3.1.1. Simulation of Damage Production by Energetic Ions

In the simulations of damage production during the sputtering process the Morse pair potential [Gi59] was used for the Al–Al interaction

$$V(r_{ij}) = D\Big\{1 - e^{-\alpha(r_{ij}-r_0)}\Big\}^2 - D, \tag{38}$$

where the parameters are $D = 0.2879$ eV, $\alpha = 1.0507$ Å^{-1} and $r_0 = 3.3218$ Å. The parameters were obtained by fitting a simulation to give correct values for the bulk cohesion energy, the compressibility and the lattice constant [As76a, Ki71]. For Ar–Al interaction potentials of Moliere (Eqs. (40) and (41)) and Ziegler *et al.* (Egs. (42)–(44)) were used and for Al–Al interaction the Lennard–Jones (6–12) potential (Eg. (45)) was used. A cutoff distance of 7 Å was used for interatomic

potentials. Particles with kinetic energies more than 5 eV were slowed down at the discrete timesteps by the friction term

$$\frac{dE}{dr_i} = -k_i\sqrt{E}, \tag{39}$$

i.e. electronic slowing down proportional to ion velocities was assumed [Fe47]. For Ar and Al ions moving in metallic aluminum k_i values of 0.0857 and 0.0212 $\sqrt{\text{eV}}\,\text{Å}^{-1}$ were used, respectively [Pu83].

The sputtering simulations were performed in a film geometry, with the film thickness enough to stop all the incident ions. Periodic boundary conditions were applied in lateral directions, with 20 atoms in each atomic plane parallel to the surface. This number of atoms in each lateral plane turned out to be sufficient for describing the damage production during the Ar^+ ion collision cascade. The total number of substrate atoms in the basic computational unit cell was around 1000. The surface layer at the back of the film was fixed to keep the sample in place. At each time t a new timestep Δt ($\geq 2 \times 10^{-16}$ sec) was incremented to correspond to a displacement of 0.1 Å of the fastest atom. The entrance position was chosen randomly above the surface far outside the potential ranges of aluminum atoms. Each Ar^+ ion was made to approach the Al (110) surface with a chosen incident polar angle with respect to the surface normal and with a fixed azimuthal angle in the <110> direction.

A typical simulation with a single Ar^+ ion of 400 eV needs about 500 timesteps and takes around 30 min CPU time on a VAX 8600 computer. For a given energy and angle of incidence, at least 100 Ar^+ ion collision cascades are needed to obtain acceptable statistics. Due to the computer limitations it was not possible to monitor the long–term recovery of the sample after each incident ion. To account for short–term recovery, a recombination radius of 4 Å for vacancy–interstitial pairs was assumed in analyzing the damage distribution. Practical computing time limits the simulations to incident Ar^+ ion energies below 1 keV. Two types of simulations were performed and they are described below.

A. Simulation of a Single Collision Cascade

In the beginning of the simulation the velocities of target aluminum atoms were selected from Maxwellian distribution. Then the target sample was allowed to stabilize to the desired equilibrium temperature ($\sim$ 300 K) during 100 timesteps. An Ar^+ ion was made to approach to this perfect crystal surface with a chosen energy and incident polar angle. After the collision cascade the produced damage data was stored for later analyses. Then the situation before the first collision cascade was restored and a second Ar^+ ion was made to approach to the perfect crystal surface. By repeating this procedure the damage data of a single Ar^+ ion incident on a perfect Al (110) crystal surface is obtained.

In these simulations the Moliere–type potential [Ro81, Va70],

$$V(r_{ij}) = \frac{C_{12}}{r_{ij}} \Phi\left(\frac{r_{ij}}{a_{12}}\right), \tag{40}$$

was used for the Ar–Al interaction, with

$$\Phi(x) = 0.35e^{-0.3x} + 0.55e^{-1.2x} + 0.10e^{-6x}. \tag{41}$$

The parameter values were chosen as $C_{12} = 234$ eVÅ and $a_{12} = 0.25$ Å.

B. Simulation of Continuous Sputtering

In this simulation collision processes were allowed to accumulate and the damage due to a "real" sputtering process were monitored. The incident energy of a few hundred eV to $\sim$1000 atom target is enough to melt the whole sample if the simulation is continued after the collision cascade. Because it is not possible to simulate the real energy reduction mechanisms, the excess energy has to be removed artificially. When all atoms had slowed down below the displacement threshold energy after the first incident Ar^+ ion, the sample was cooled down to the initial temperature before a new collision cascade by gradually decreasing (rescaling) the atomic velocities during 200 timesteps. The second Ar^+ ion was then allowed to

approach the already damaged sample. This procedure was continued until the desired sputtering dose was achieved.

In these simulations the universal potential of Ziegler *et al.* [Zi85] was used for Ar–Al interaction

$$V_u(r_{ij}) = \frac{Z_1 Z_2 e^2}{r_{ij}} \Phi_u \left(\frac{r_{ij}}{a_u} \right), \tag{42}$$

where

$$\Phi_u(x) = 0.1818e^{-3.2x} + 0.5099e^{-0.9423x} + 0.2802e^{-0.4028x} + 0.02817e^{-0.2016x} \tag{43}$$

and

$$a_u = \frac{0.8854\, a_0}{Z_1^{0.23} + Z_2^{0.23}}. \tag{44}$$

Above a_0 is the Bohr radius and Z_1 and Z_2 are the atomic numbers of Al and Ar atoms, respectively.

3.1.2. Simulation of Surface Melting

The structural properties of the surfaces of an FCC Lennard–Jones system has been studied by the molecular dynamics simulation methods. For the atomic interaction the well known Lennard–Jones pair–potential [As76a] is used

$$V(r_{ij}) = 4\epsilon \left\{ \left(\frac{\sigma}{r_{ij}} \right)^{12} - \left(\frac{\sigma}{r_{ij}} \right)^{6} \right\}, \tag{45}$$

where the parameters ϵ and σ are characteristic of each noble gas. For argon the parameters are $\sigma = 3.40$ Å and $\epsilon = 0.0104$ eV [Be58], and the corresponding time parameter is $\tau = (m\sigma^2/\epsilon)^{1/2}$. A cutoff distance of $\sim 3\sigma$ is used.

The simulations have been performed as follows. First the equilibrium condition at zero pressure is calculated for a bulk system of 864 atoms as a function of temperature. Periodic boundary conditions have been imposed on the computational unit cell in each direction. Density (volume) and temperature scaling are allowed and the simulation is continued until the sample is stabilized to the

desired temperature. The calculated density vs. temperature curve has been used thereafter to obtain correct densities for the surface melting simulations.

Surface melting is studied in a film geometry, where periodic boundary conditions are imposed in two directions. The thickness of the film is 13 atomic planes; 1040 atoms are included in the basic computational unit cell (80 atoms in each atomic plane parallel to the surface). Thus a statistics of 160 atoms is achieved for the analysis of each near–surface layer. The system is initially equilibrated at temperature $T = 0.42\epsilon$ and at a density corresponding to the bulk sample in zero pressure. Then the bulk temperature vs. density curve (bulk P=0 isobar) is followed by increasing the temperature and decreasing the density in small steps. At each temperature 2000 timesteps of 0.0093τ were simulated to achieve an equilibrium condition.

3.2. DAMAGE PRODUCTION IN SPUTTERING OF Al (110) SURFACE WITH SLOW ARGON IONS

A series of computer simulations has been performed to investigate the damage production in Al (110) surface with 200 and 400 eV argon ion bombardment. Two types of calculations are carried out: In Chapter 3.2.1. the damage production due to single collision cascades is described. This gives the maximum damage production per incident Ar^+ ion and corresponds to sputtering at low doses (one Ar^+ ion per 20 surface atoms, $\sim 4.3 \times 10^{13}$ ions/cm^2). In Chapter 3.2.2. the simulation of a continuous sputtering is described. In these simulations the sample is cooled after each Ar^+ ion collision cascade but the sputtering effects are allowed to accumulate. Simulations are continued until the energy of the fastest atom is below the displacement threshold energy. Thus the maximum rate of damage production is monitored during sputtering. Also the recovery of a sputtered sample is investigated by continuing the simulation of high Ar^+ ion dose (8.6×10^{14} ions/cm^2) of E $=$ 400 eV and $\theta = 25°$ with an equilibrium simulation.

3.2.1. Damage Produced by a Single Ar^+ Ion

A qualitative test for the simulation is the obtained sputtering yield. The calculated sputtering yields are shown as a function of the incident angle, θ, for two Ar^+ ion energies in Fig. 41. The yield increases with the incident angle from 0° to 45° and then decreases for larger angles. At 200 eV, Ar^+ ions reflect totally from the single crystal Al (110) surface when $\theta > 75°$. This is expected, as the kinetic energy perpendicular to the surface is of the same order of magnitude or less than the threshold energy for sputtering [St62]. The sputtering yield is of

the same order of magnitude for both Ar–Al potentials. It is a little higher from a perfect lattice structure than from a sputtered one. This is expected, because an ion can penetrate deeper into damaged material before the first collision than to the perfect crystal and most of the ejected atoms come from the surface layer [Bi84, Sh85]. The agreement between calculated and experimental [We67, An81, La61, Oe73] sputtering yields is satisfactory. Also the overall behaviour of the simulated sputtering yield as a function of the incident angle of Ar^+ ions is in agreement with corresponding experimental results [Oe73, Ve80]. However, one should note that a more realistic cutoff energy for the sputtering process is the surface binding energy rather than the displacement threshold energy relevant for vacancy–interstitial production. Here the main interest is the damage production in sputtering.

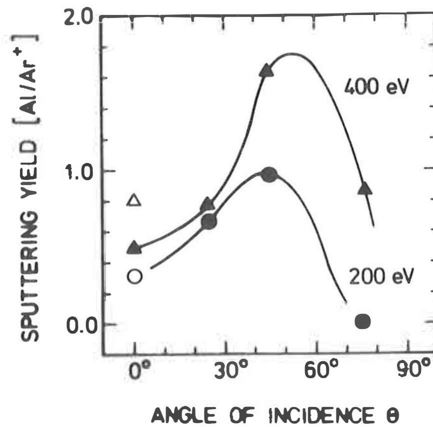

Fig. 41. Sputtering yield from Al (110) as a function of the incident angle θ for Ar^+ ion energies of 200 and 400 eV. The closed marks denote the molecular dynamics simulation and the open symbols experimental results from [We67]. The lines are drawn just to guide the eye.

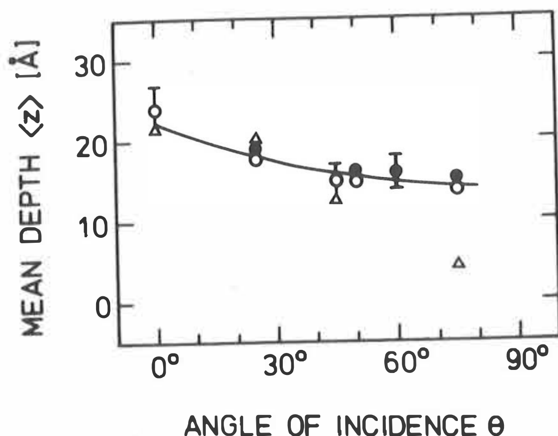

Fig. 42. The mean vacancy concentration depth <z> as a function of the incident angle θ of Ar^+ ions in sputtered Al (110). Triangles denote the molecular dynamics calculation for 400 eV Ar^+ ions. Open and closed circles are experimental mean damage concentration depth values [Mä86] for 400 and 800 eV Ar^+ ion energies, respectively.

The mean depth of the produced vacancies is almost independent on the Ar^+ ion energy and dose below a few keV (Fig. 42). The incident Ar^+ ion loses its kinetic energy to the topmost atomic layers and the energy spreads out near to the surface, which is in agreement with other simulations [Is74, Ja86]. The mean depth decreases as a function of the incident angle. 400 eV Ar^+ ions reflect almost totally from the perfect crystal surface at $\theta = 75°$ and produce only a few defects near to the surface (simulated points in Figs. 42 and 43). If the aluminum surface is already roughened before the incidence of an Ar^+ ion, as is the case in experiments, the ions are able to penetrate deeper in the material also at large incident angles and they will produce defects deeper in the material.

The number of produced vacancies per incident ion is in qualitative agreement with collision cascade simulations [Er65]. The maximum vacancy production rate per incident Ar^+ ion occurs around the incident angle $\theta = 45°$ as can be seen

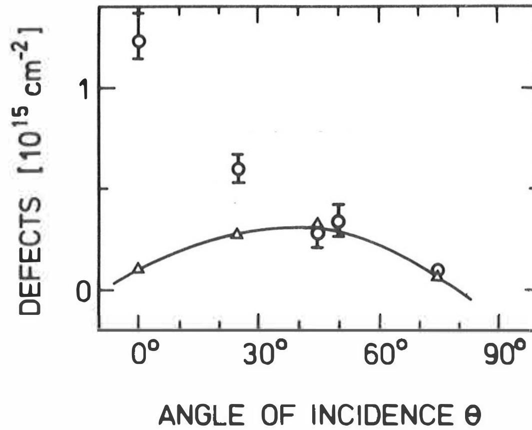

Fig. 43. The total number of vacancies vs. the incident angle θ of 400 eV Ar^+ ions in sputtered Al (110). Triangles denote the molecular dynamics calculations (low Ar^+ ion dose) and circles are experimental total numbers of defects corresponding to saturated damage concentration [Mä86].

from the simulated values in Fig. 43. Only few defects per incident Ar^+ ion are produced at small angles θ due to the effective channeling of argon atoms toward <110> direction (simulated data in Fig. 43). On the other hand, they are deeper in material due to channeling and the total number of defects will accumulate during further sputtering. It reaches a saturation value, when the Ar^+ ion dose is increased to $\sim 2 \times 10^{14}$ ions/cm^2 (Fig. 44).

3.2.2. Continuous Sputtering

The total number of defects increases as a function of Ar^+ ion dose and reaches a saturation value, when a couple of atomic layers have been sputtered off (Fig. 44). At small Ar^+ doses the agreement between simulations and experiments performed at 150 K (vacancies not mobile) is good. At higher doses the disorder in the sample saturated during the simulation and the sample started to recover by the enhanced recombination of vacancies and interstitials during further sputtering. The simulated vacancy concentration saturated at high Ar^+ dose to around 0.6×10^{-15} vacancies per cm^2, which is of the same order of magnitude than the experimental value [Mä86].

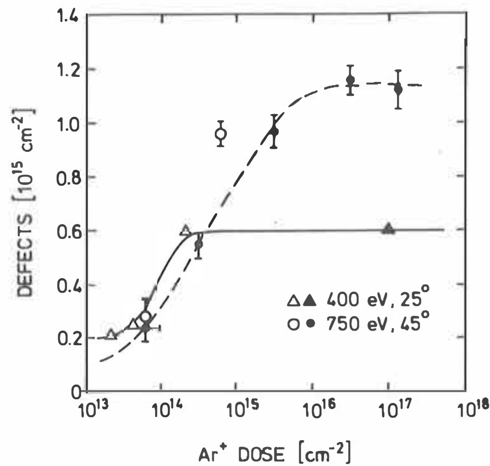

Fig. 44. The total number of vacancies as a function of Ar^+ ion dose. Open triangles denote the molecular dynamics calculations and the solid triangle is an experimental point [Mä86]. Open and closed circles are from experiments [Mä86] done at 150 and 300 K, respectively. The lines are drawn just to guide the eye.

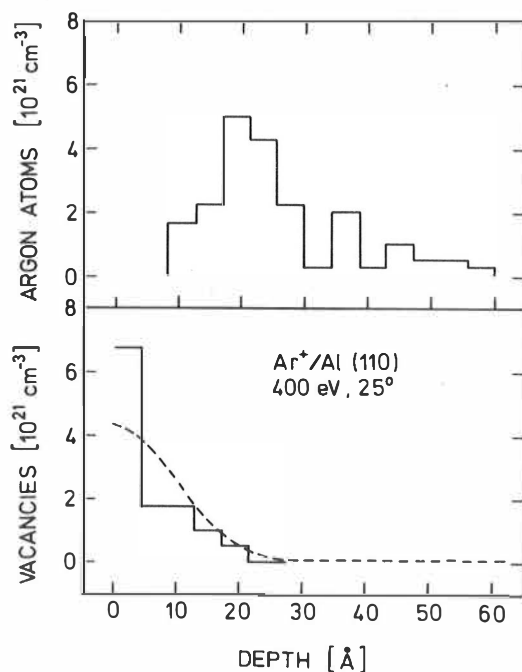

Fig. 45. Argon implantation and vacancy profiles in argon sputtered Al (110). A recovery of 6000 timesteps ($\sim 5 \times 10^{-11}$ seconds) is continued after the simulation of a fluence of 8.6×10^{14} Ar^+ ions per cm^2. No recombination radius is used for vacancy–interstitial pairs in analysis. Each bar corresponds to three atomic layers. The dashed line is an experimentally deduced high Ar^+ dose (fluence–independent) defect profile [Mä86].

Molecular dynamics calculations of the vacancy profiles agree with the overall shape of the experimentally extracted damage distributions [Mä86]. The interstitial and projectile particle profiles are clearly deeper in material than the vacancy profiles. An argon implantation profile and a vacancy profile together with the experimentally determined damage profile are shown in Fig. 45 for Ar^+ ions of initial energy 400 eV and of incident angle 25°. After the entrance of 20 Ar^+ ions (8.6×10^{14} ions/cm^2) to the target a recovery of 6000 timesteps (in total 5×10^{-11} sec) was carried out. This time is enough to reach a quasi–equilibrium

situation [We83b, Ha83b]. A clear diffusive motion of interstitials and vacancies was noticed; the mean depth of vacancies decreased and interstitials increased by ~ 3 Å. This is due to the recombination in the area, where the initial distributions overlapped. The simulated Ar^+ ion ranges and distributions are in agreement with experimental values [Si86, Do64]. The mean depth of implanted argon ions increased only by 0.7 Å during the recovery and quite a compact layer of argon atoms was produced in aluminum. This is in agreement with the earlier observed formation of vacancy–argon complexes by van Veen *et al.* [Ve82].

3.3. PREMELTING OF NOBLE GAS (111) SURFACES

The structure of crystal surfaces close to but below the bulk melting temperature has been a subject of wide interest during the past decade. Especially the occurrence of premelting phenomena has been investigated intensively [Br78, Br83a, Br83b, Po85, Ro86, Sc85, Ja85, Ho85, La86, Fr85, Fr86]. Lipowsky [Li82, Li84, Li86] has given general arguments about surface phenomena at first order bulk transitions: a layer of disordered phase intervenes between the surface and ordered bulk. The mechanisms and phenomena associated with the disordering of surfaces below the bulk melting temperature have been examined by molecular dynamics simulations, but no general agreement exists about whether real melting of surface layers takes place or merely disordering (roughening) is the dominating mechanism.

The most frequently used model for describing the interactions between solid noble gas atoms is the Lennard–Jones (LJ) potential. The overall behaviour of Lennard-Jones surfaces is known quite well from the molecular dynamics simulations of Broughton *et al.* [Br78, Br83a, Br83b]. Recently Rosato *et al.* [Po85, Ro86] have presented results of a more detailed molecular dynamics simulation for the Lennard-Jones (110) surface. Their conclusion is that the only disordering mechanism below the bulk melting point is surface roughening. On the other hand, surface premelting has been observed in the earlier simulations [Br78, Br83a, Br83b]. Furthermore, the potential of Barker *et al.* [Ba74], which is considered to be more realistic for noble gases than the Lennard–Jones potential, is supposed to result in an even more pronounced premelting [Sc85]. Premelting phenomena at surfaces and interfaces have been observed also in simulations for other systems [Ja85, Ho85, La86]. For example, in crystalline silicon melt fronts have been found both experimentally and by molecular dynamics simulations to proceed along the directions of high packing density [La86].

The first report of direct experimental observation of surface premelting was published in 1985 by Frenken *et al.* [Fr85, Fr86]. They performed ion–scattering measurements on an atomically clean Pb (110) surface and found the presence of a liquid surface film on top of the well ordered substrate. The surface melting took place at around 40 K below the bulk melting point T_m and the melt front progressed continuously into the material, when temperature was further raised towards T_m. Roughening of the Cu (110) surfaces below the bulk melting temperature has been observed experimentally by Mochrie [Mo87]. He concluded that roughening takes place only on the loosely packed Cu (110) surfaces but not on the more densely packed (111) and (100) surfaces. Surface roughening and melting transitions below the bulk melting temperature have also been observed on argon multilayers adsorbed on graphite [Zh86].

In Chapter 3.3.1. the statistical accuracy of the molecular dynamics simulations is discussed. The results of the calculations and comparison with experimental data are presented in Chapter 3.3.2. A concluding discussion is given in Chapter 3.3.3. In the following the coordinates x and y are defined parallel to the surface and the coordinate z in the direction perpendicular to the surface. Furthermore, layer 1 is defined for the outermost atomic plane, layer 2 for the plane just below, and so on. The Lennard–Jones parameters ϵ and σ are characteristic of each noble gas. Therefore, in the following the unit σ is used for length, ϵ for energy (and temperature) and $\tau = (m\sigma^2/\epsilon)^{1/2}$ for time.

3.3.1. Reliability of Thin Film Calculations

In molecular dynamics simulations one is always forced to make compromises as has been discussed earlier in Chapter 3.1. When the time necessary to follow atomic trajectories is known the maximum feasible number of atoms in the basic computational unit cell is stated by the computer recourses in use. When the

surface properties of a thin film are studied, the final compromise is between the statistical accuracy of parameters describing the properties of surface layers and the film thickness. The film must be thick enough so that its surfaces behave in the same way than for a semi-infinite system, but as thin as possible to achieve a reasonable statistics (large number of atoms in the lateral direction).

The validity of molecular dynamics simulations of surface melting by using film thicknesses around 13 atomic planes has been criticized by Rosato *et al.* [Ro86]. They argue that for describing surface phenomena correctly the film must be around 50 atomic planes thick, if each atomic plane parallel to the surface contains 48 atoms. Their criterion is that the mean total energy per atom in the sample should correspond to bulk (experimental) values.

It is true that the mean total energy per atom in thin films differs clearly from the bulk value. The bulk limit is approached with increasing film thickness, as the weight of the surface atoms in calculating the mean total energy per atom decreases. Atoms in the surface layers have higher total energies than atoms in the bulk, because part of the interatomic bonds are missing near the surface. The total energy of the (111) surface atoms is higher than in the bulk by approximately 2.5ϵ. This increases appreciably the mean total energy per atom for thin films, but the energy distribution near the surface does not change in z–direction from the one for thick films.

The sufficient criterion for the minimum film thickness is that the mean total energy per atom in the middle of the film is similar to the experimental value. Fig. 46 demonstrates the effect of the surface layers on the mean total energy per atom. The total energy per atom for the five atomic planes in the middle of the film is much closer to the experimental data than the mean value for the whole sample (13 atomic planes thick). In the present simulation the remaining difference decreases the simulated melting temperatures by a few degrees from the experimental ones. The use of films over 20 planes thick would give melting

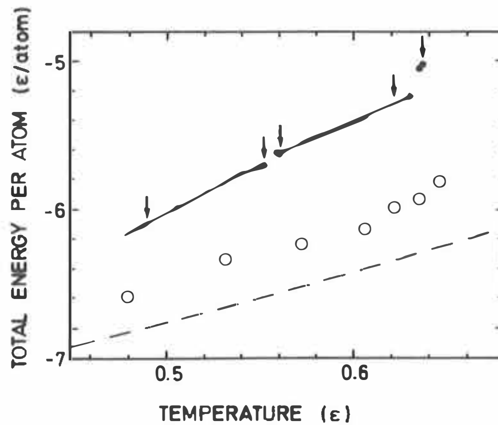

Fig. 46. Total energy per particle as a function of temperature for argon with (111) surfaces. Full circles are the mean values over the whole sample and open circles the mean values of atoms in the five layers in the middle of the film. The density of the sample at each temperature corresponds to the bulk density at zero pressure ($P = 0$ isobar). The dashed line shows the experimental argon data [Ga76]. Temperatures marked by arrows are analyzed in greater detail down below.

temperatures close to experiment, but the increase of the film thickness would not change the qualitative behaviour of the surfaces. This is actually seen in the paper of Rosato *et al.* [Ro86], where the simulations with film thicknesses of 14 and 56 atomic planes gave practically equal results for the (110) surface. The difference between the mean total energy of atoms in the middle of the film and the experimental bulk values stays constant with temperature (Fig. 46), which indicates that a bulk driven surface melting does not take place.

3.3.2. Premelting of Lennard–Jones (111) Surfaces

The total energy per atom as a function of temperature is shown in Fig. 46. A small jump in the total energy is observed around $T \approx 0.56\epsilon$. This is due to the melting of the surface atomic planes (layer 1). At $T \approx 0.63\epsilon$, where the second layer melts, a more distinct jump in the total energy is seen. The reason is that the melting transition of the first layer takes place on a crystal–vapor interface, where atoms are more loosely bound than those deeper in the material. The melting transition of the second layer resembles rather a transition on a crystal–liquid interface. Similar behaviour in the total energy vs. temperature curve has been observed also for LJ (100) surfaces [Br78]. The melting temperature for the (100) surface is lower than that for the (111) surface, because a loosely packed surface disorders more easily than a densely packed one. The bulk melting temperature is $T_m \approx 0.696\epsilon$ [Wea83].

Lennard–Jones surfaces relax outwards, in accordance with earlier results [Br83a, Al69]. The amount of surface relaxation decreases as a function of packing density from (110) to (100) to (111). This is qualitatively obvious, because the LJ–potential is repulsive at the nearest neighbour distance and the packing density of a surface layer is inversely proportional to the number of nearest neighbours down below the surface layer for an atom in the surface layer. The relaxations of the (110) and (100) surface layers are around 7 %, but for the (111) surface it is only half of that. The relaxation of the second layer of the (111) surface is around 1 % ; the relaxations of layers deeper in the material are insignificant. No experimental data exists for the relaxation of noble gas surfaces.

Trajectory plots of atoms, projected onto the yz–plane, are shown in Fig. 47 and the trajectories of atoms in the first layer are shown in Fig. 48 for temperatures indicated in Fig. 46. Vacancy formation in the first layer starts at low

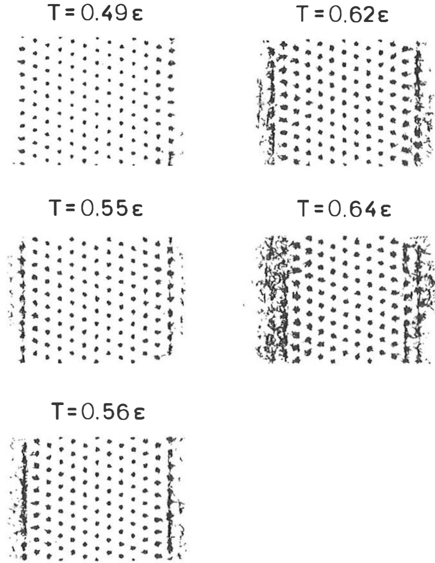

Fig. 47. Trajectories of atoms in the whole unit cell projected to a plane perpendicular to the surface (yz–plane) for temperatures marked by arrows in Fig. 46. When an atom crosses a boundary of the computational unit cell (in x– or y–direction), its trajectory is continued on the other side of the box due to the periodic boundary conditions.

temperatures, $T \leq 0.49\epsilon$, and the layer melts at $T \approx 0.56\epsilon$. The second layer is preserved in a crystalline order until the melt front penetrates deeper at $T \approx 0.63\epsilon$. The crystalline structure below $T \approx 0.56\epsilon$ can be seen in the xy–trajectory plots of atoms in the first layer, but at higher temperatures the layer is clearly disordered.

The mean square displacement of N_l atoms, initially in the lth layer at time $t = 0$, is

$$\langle \Delta r^2 \rangle = \frac{1}{N_l} \sum_{i=1}^{N_l} [\overline{r}_i(0) - \overline{r}_i(t)]^2. \tag{46}$$

The mean square displacements as a function of time for layers 1, 2, and 7, and for temperatures indicated in Fig. 46, are shown in Fig. 49. At temperature $T \approx 0.49\epsilon$, atoms merely oscillate around their lattice sites. Atoms in the first

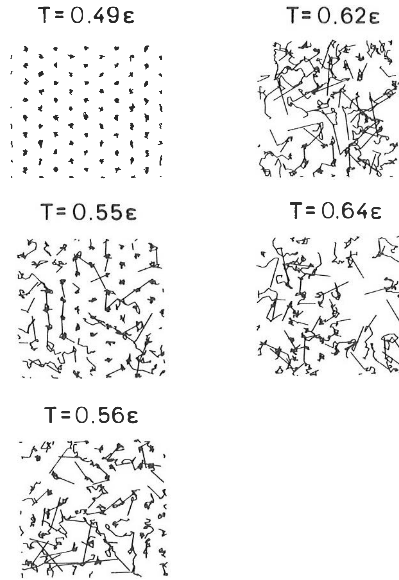

Fig. 48. Trajectories of atoms in the first layer for temperatures marked by arrows in Fig. 46. The starting point of each atom is inside the surface layer. When an atom crosses a boundary of the computational unit cell (in x– or y–direction), its trajectory is continued on the other side of the box due to the periodic boundary conditions.

layer are expected to move more freely than atoms in the bulk, because the surface binding energy of an atom is approximately half of the cohesion energy for atoms in the bulk. When the temperature is increased to $T \approx 0.55\epsilon$, the mean square displacement of atoms in the first layer increases more rapidly as a function of time. This is due to the increased vacancy formation in the surface layer. Atoms in the first layer are able to jump from their equilibrium sites on the surface and also to vacant atomic sites in the layer, but the surface atoms still spend most of their time around the lattice sites. The mean square displacement of atoms in the first layer increases considerably during the melting transition and the increase as a function of time is linear above $T \approx 0.56\epsilon$. However, the mean

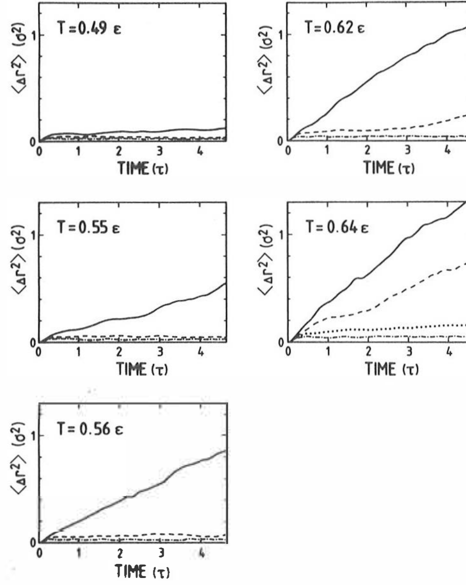

Fig. 49. Mean square displacement of atoms as a function of time for temperatures marked by arrows in Fig. 46. The solid line corresponds to the first layer, the dashed line to the second layer, the dotted line to the third layer, and the dot–dashed line to the 7th layer (the layer in the middle of the film).

square displacement of atoms in the second layer stays constant as a function of time. This means that the second layer clearly remains solid and no transition takes place. The mean square displacement in the second layer increases after the melting starts to proceed deeper in the material around $T \approx 0.63\epsilon$, but the third layer remains still ordered. The mean square displacement of atoms in the 7th layer corresponds to the thermal vibration of atoms in a solid structure.

The two dimensional diffusion coefficient in layers parallel to the surface is obtained by

$$D_{xy} = \frac{\frac{1}{N_l}\sum_{i=1}^{N_l}\left\{[x_i(t) - x_i(0)]^2 + [y_i(t) - y_i(0)]^2\right\}}{4t}, \quad t \longrightarrow \infty. \tag{47}$$

All atoms moving from one layer to another are excluded from this correlation function. The linear part of the two–dimensional mean square displacement vs. time curve is used to calculate an estimate for D_{xy}. The obtained diffusion coefficients for the first and the second layer are presented in Fig. 50 as a function of temperature.

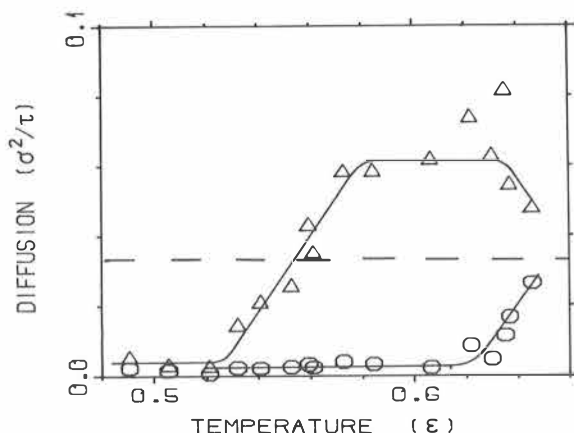

Fig. 50. Two-dimensional diffusion coefficients of layers 1 (△) and 2 (◯) as a function of temperature. The dashed line is an experimental bulk diffusion coefficient of liquid argon near the triple point [Na62].

The two–dimensional self–diffusion constant in the first layer increases between $T \approx 0.52\epsilon - 0.56\epsilon$ from a solid value to around $0.06\sigma^2/\tau$, which is twice the experimental bulk liquid value [Na62]. As in other simulations [Br83b], the diffusion coefficient is found to be higher at the surface (layer 1) than in the bulk liquid. The diffusion coefficient in the second layer stays low until the temperature $T \approx 0.63\epsilon$ is reached, where the second layer melts. The diffusion coefficient for the second layer increases only up to $\sim 0.03\sigma^2/\tau$, which is of the same order of magnitude as the experimental bulk liquid value. The reason for this is that the conditions in

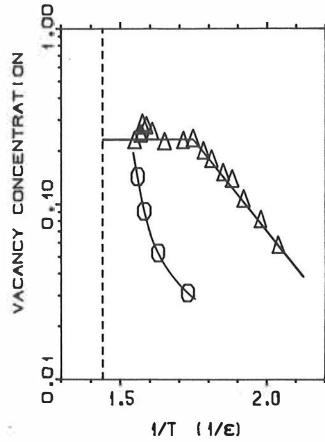

Fig. 51. Arrhenius plots for the vacancy concentration for layers 1 (△) and 2 (○). The dashed line corresponds to the experimental melting temperature of solid argon [Ga76].

the second layer correspond more to a liquid phase, because it is between a very mobile liquid surface layer, and the solid third layer on the other side.

The increased vacancy formation in layers 1 and 2 as a function of temperature is shown in the Arrhenius plots for vacancy concentration in Fig. 51. The vacancy concentration in the first layer starts to increase around $T \approx 0.5\epsilon$ and it saturates at $T \approx 0.56\epsilon$ to a value of about 0.25. The vacancy concentration in the second layer starts to increase near the temperature at which it saturates in the first layer. The vacancy concentrations at the studied temperatures are statistically negligible in layers deeper in the material. It obviously saturates in the second layer before any substantial vacancy formation begins in the third layer. This is a clear indication of a disorder that proceeds layer–by–layer.

The observed saturation for the vacancy concentration in the first layer implies that its structure changes when the temperature is increased. The simulated vacancy concentrations for the (111) surface layers are also in good agreement with

the earlier simulation [Br83a] for temperatures below $T = 0.6\epsilon$. The behaviour of the vacancy concentration in the (100) surface layers [Br83a] is qualitatively similar to the behaviour in the (111) surface layers. In the (110) surface the vacancy concentration increases simultaneously at least in two layers and no saturation has been observed [Br83a, Po85, Ro86].

The free energy for the vacancy formation f_v in the first layer can be approximated from the slope of the vacancy concentration c_v as a function of inverse temperature $1/T$ as

$$c_v = \exp\left(-\frac{f_v}{k_B T}\right), \tag{48}$$

where k_B is the Boltzmann constant. Temperature dependence of f_v is given by $f_v = \epsilon_o - \alpha k_B T$, where ϵ_o is the vacancy formation energy and αk_B the vacancy formation entropy. From Fig. 51 one obtains that $\epsilon_o \approx 4.5\epsilon$ and $\alpha \approx 6.5$.

Also the two–dimensional order parameter, defined as

$$S_{xy} = \frac{1}{2N_l} \sum_{i=1}^{N_l} \left[\cos\left(\frac{2\pi}{a_x} x_i\right) + \cos\left(\frac{2\pi}{a_y} y_i\right)\right], \tag{49}$$

has been calculated for layers parallel to the surface. Above N_l is the number of atoms in the lth layer and a_x and a_y are the FCC interatomic distances in the x– and y–directions, respectively. This order parameter has the value 1 for a perfect crystal at $T = 0$ and 0 for a fully disordered material.

The calculated order parameter for the first layer decreases continuously above $T \approx 0.48\epsilon$ and obtains a value corresponding to the liquid phase around $T = 0.56\epsilon$ (Fig. 52). For layers deeper in the material, the temperature dependence of the order parameter becomes quickly much steeper. This is in accord with the Landau picture of first order bulk transitions near interfaces [Li82, Li86]. Conclusion is that the first layer disorders just above $T \approx 0.56\epsilon$, and the diffusion studies show that atoms are moving around within that layer. The simultaneous increase of the diffusion coefficient (Fig. 50), the saturation of the vacancy concentration (Fig. 51) and the loss of order (Fig. 52) in the first layer confirm that a melting transition takes place in the surface layer far below the bulk melting temperature.

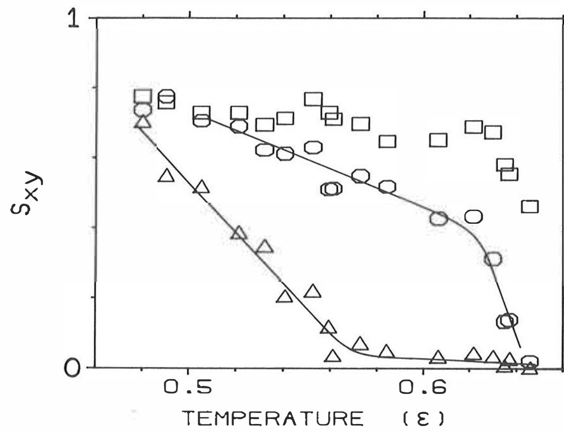

Fig. 52. The two–dimensional order parameter for layers 1 (△) and 2 (○) and the five layers in the middle of the film (□) as a function of temperature.

3.3.3. Discussion

All the performed analyses support the conclusion that premelting of the Lennard–Jones (111) surface layers takes place far below the bulk melting temperature. The first layer melts at the lowest temperature, and the melting temperature increases with the layer number. Melting of the first two surface layers was observed. This agrees with Lipowsky's theory [Li84] according to which a molten surface layer has a maximal thickness, which depends on the sample size. It can be concluded that melting proceeds via a layer–by–layer mechanism, at least in the (111) direction. This study, together with the earlier results [Br78, Br83a, Br83b, Po85, Ro86, La86], supports the finding that melting proceeds along the directions of high packing densities.

After a survey to the numerous molecular dynamics simulation studies on the melting processes (see e.g. [Br78, Br83a, Br83b, Po85, Ro86, La86]), it is clear that the loosely packed (110) faces of Lennard–Jones FCC crystals disorder at a

lower temperature than the more densely packed (100) faces, and the most densely packed (111) faces disorder at the highest temperature. The transition proceeds via a layer–by–layer mechanism also on (110) and (100) faces, at least for the sample sizes feasible in molecular dynamics simulations. However, no agreement exists in literature about the disordering mechanisms: should the transition be called melting or roughening, when does the surface melting or roughening take place, etc. Also the use of term roughening is somewhat confusing. Molecular dynamics simulations can describe only small scale phenomena, where no really rough surface structures have been observed. Therefore, should a process found by molecular dynamics simulations be called roughening transition at all, even if the surface structure on a larger scale, far beyond the molecular dynamics simulations, might be rough? Of course, the initial surface orientation affects the roughening of large scale structures, and molecular dynamics simulation can show precursor effects to large–scale roughening. Thermodynamically, roughening should be defined as the disappearance of the free energy associated with the formation of a surface step. The corresponding roughening temperature is typically above the melting temperature.

The increase of the vacancy concentration in the surface layers is associated with the increase in the mobility of surface atoms. This does not necessarily mean that there exists a molten layer at the surface, as emphasized by Rosato *et al.* [Po85, Ro86] for Lennard–Jones (110) surfaces. In the case of the (110) surfaces the mobility of atoms near the surface is increased mainly in the direction perpendicular to the surface. However, in the case of the (111) surfaces the mobility of atoms is highest in directions parallel to the surface and quite small in the perpendicular direction. This results in a formation of a liquid film on the surface below the bulk melting temperature. This surface–initiated melting, if generally present at close–packed surfaces, is a natural explanation for the absence of superheating in solids.

4. SUMMARY

Monte Carlo and molecular dynamics simulation methods have been applied to study different surface and near–surface phenomena. 1–10 keV electron and positron slowing down in solids has been simulated by Monte Carlo methods. Elastic processes are described by accurate single–atom scattering cross sections in solid material, ionization processes are described by Gryzinski's semi–empirical formula, and excitation processes are included by an approximation so that the total electronic stopping power agrees with the Bethe formula at high energies.

Good agreement is obtained between the Monte Carlo and experimental electron transmission and backscattering probabilities and positron transmission probabilities. Positron backscattering probabilities from different materials are found to be considerably smaller than those for electrons. 1–10 keV electron and positron penetration properties differ distinctly from the higher energy values. The mean penetration and energy deposition depths follow the familiar exponential formula $\overline{z} = \alpha E^n$, where α, in units of g/cm^2, increases only a little as a function of atomic number of the target material. But the stopping profile is a negative of the derivative of a Gaussian function and not an exponentially decreasing one as supposed earlier on the basis of high energy data. The energy deposition profile is a Gaussian one as has been estimated on the basis of experimentally deduced ionization profiles. The energy deposition and ionization profiles are in practice identical (in particular for the weakly bound electrons). Analytic fits are presented for the stopping and energy deposition profiles. Laplace transforms of positron implantation profiles should be useful in analyzing positron re–emission data.

A series of molecular dynamics simulations of Ar^+ sputtering damage near an Al (110) surface has been performed. Interactions between aluminum atoms are described by the Morse potential, the Ar–Ar interactions by the Lennard–Jones potential, and the Ar–Al interactions both by the Moliére potential and

the universal potential of Ziegler *et al.* Electronic slowing down proportional to ion velocities is included. Calculations show that the obtained vacancy profiles contain a narrow peak within the topmost atomic layers, followed by a broader tail. The interstitial and argon atom distributions are much more spread out at larger depths. The simulated damage profiles at high Ar^+ ion dose are consistent with the experimental results and give indication of the formation of the vacancy–argon complexes. The defect production rate at low Ar^+ ion doses and small incident angles is much smaller than at large angles, but increases considerably as a function of the sputtering dose. These phenomena are apparently connected to the channeling of argon atoms toward the <110> direction.

Premelting of noble gas surfaces is also simulated by molecular dynamics methods. Noble gas surfaces are described by the frequently used Lennard–Jones potential and qualitative agreement is obtained with earlier studies. Lennard–Jones (111) surfaces are studied in more detail and a complete view of the disordering of Lennard–Jones surfaces as a function of temperature is obtained. Premelting of the (111) surfaces takes place far below the bulk melting temperature. The first layer starts to disorder by vacancy formation and when the vacancy concentration saturates to ~25 % at $T = 0.56\epsilon$ the layer melts, but the second layer is still in crystalline order. The melt fronts proceed into the material via a layer–by–layer mechanism, when the temperature is further increased. LJ (100) surfaces behave similarily as a function of temperature than the (111) surfaces, but the disordering of LJ (110) surfaces is more like a roughening transition. The observation that melting proceed along the directions of high packing densities is in agreement with the earlier experimental and theoretical results for other materials (e.g. silicon).

APPENDIX

Schematic flow chart of the Monte Carlo simulation.

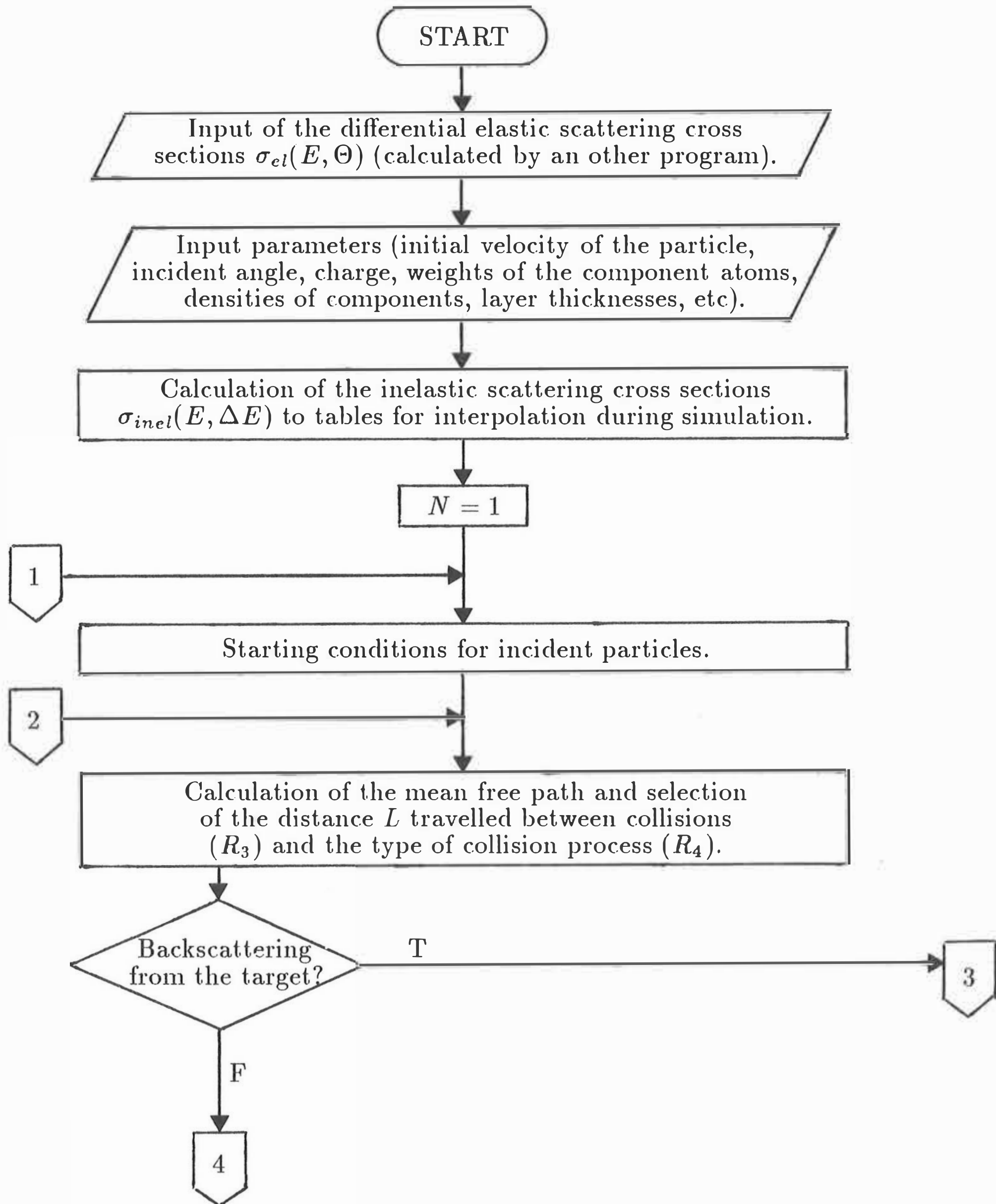

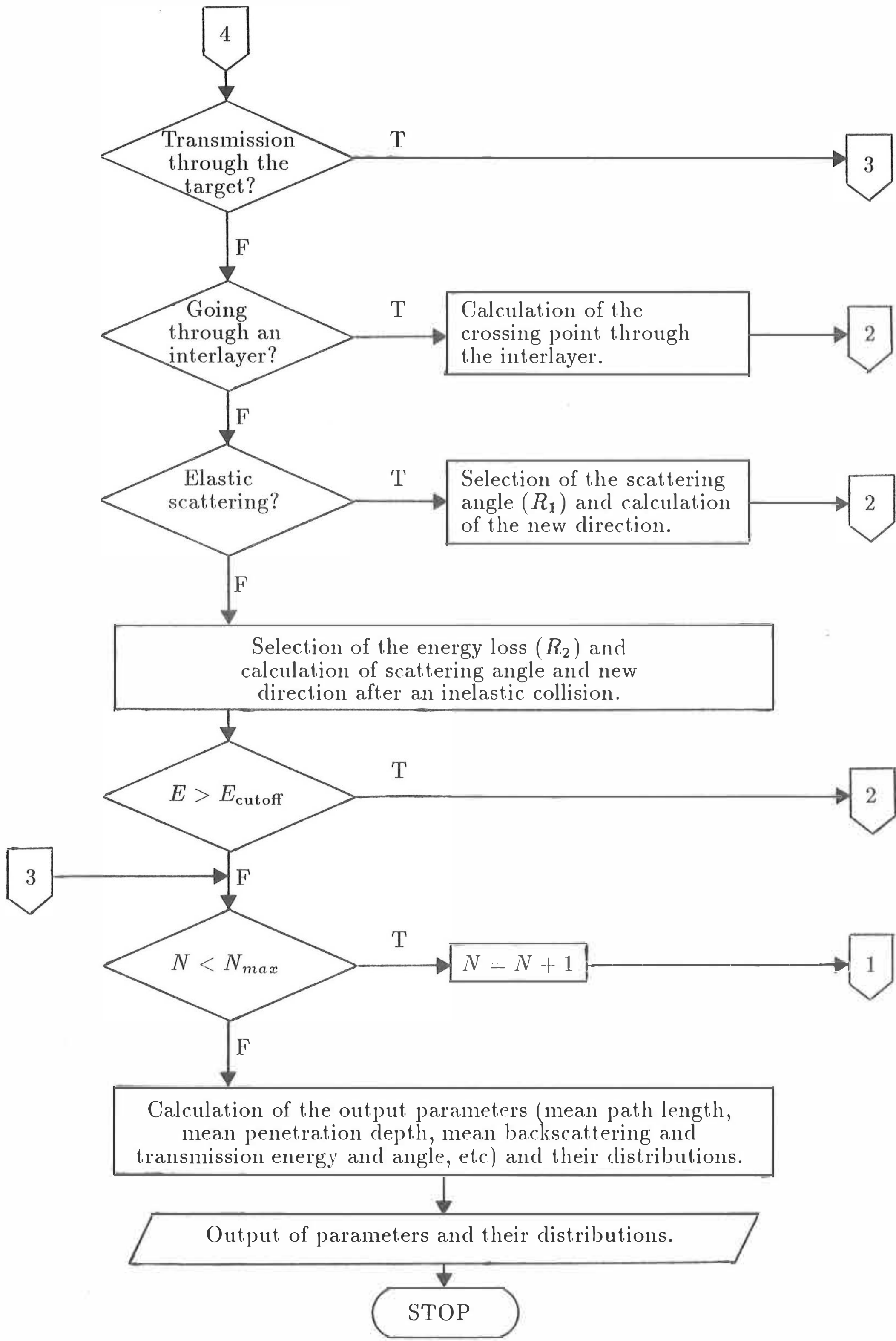
4
Transmission through the target?
T
3
F
Going through an interlayer?
T
Calculation of the crossing point through the interlayer.
2
F
Elastic scattering?
T
Selection of the scattering angle (R_1) and calculation of the new direction.
2
F
Selection of the energy loss (R_2) and calculation of scattering angle and new direction after an inelastic collision.
$E > E_{\text{cutoff}}$
T
2
3
F
$N < N_{max}$
T
$N = N + 1$
1
F
Calculation of the output parameters (mean path length, mean penetration depth, mean backscattering and transmission energy and angle, etc) and their distributions.
Output of parameters and their distributions.
STOP

REFERENCES

[Ab65] M. Abramowitz and I. A. Stegun, Handbook of Mathematical Functions (Dover, New York, 1965).

[Ad80] A. Adams and P. K. Hansma, Phys. Rev. B **22** (1980) 4258.

[Al69] R. E. Allen, F. W. de Wette, and A. Rahman, Phys. Rev. **179** (1969) 887.

[An81] H. H. Andersen and H. L. Bay, in "Sputtering By Particle Bombardment I", ed. R. Behrisch, Topics in Applied Physics **47** (Springer, 1981) p. 145.

[An87] H. H. Andersen, Nucl. Instr. Meth. **B18** (1987) 321.

[As76a] N. W. Ashcroft and N. D. Mermin, Solid State Physics (Holt, Rinehart and Wiston, New York, 1976).

[As76b] J. C. Ashley, C. J. Tung, R. H. Ritchie, and V. E. Anderson, IEEE Trans. Nucl. Sci. **NS-23** (1976) 1833.

[As79] J. C. Ashley, C. J. Tung, and R. H. Ritchie, Surf. Sci. **81** (1979) 409.

[Ba74] J. A. Barker, R. O. Watts, J. K. Lee, T. P. Schafer, and Y. T. Lee, J. Chem. Phys. **61** (1974) 3081.

[Ba76] J. L. Barrett and P. B. Hays, J. Chem. Phys. **64** (1976) 743.

[Be81] R. Behrisch (ed.), Sputtering by Particle Bombardment I, Topics in Applied Physics **47** (Springer, 1981).

[Be83] R. Behrisch (ed.), Sputtering by Particle Bombardment I, Topics in Applied Physics **52** (Springer, 1983).

[Be76] D. Beeman, J. Comp. Phys. **20** (1976) 130.

[Be70] M. J. Berger, S. M. Seltzer, and K. Maeda, J. Atmos. Terr. Phys. **32** (1970) 1015.

[Be82] M. J. Berger and S. M. Seltzer, Stopping Powers and Ranges of Electrons and Positrons (U. S. Department of Commerce, National Bureau of Standards, Washington, 1982).

[Be58] N. Bernardes, Phys. Rev. **112** (1958) 1534.

[Be33] H. Bethe, in "Handbuch der Physik", vol. 24, eds. H. Geiger and K. Scheel (Julius Springer, Berlin, 1933) p. 491.

[Be53] H. A. Bethe and J. Ashkin, in "Experimental Nuclear Physics", ed. E. Segré (Wiley, New York, 1953) p. 278.

[Bi84] J. P. Biersack and W. Eckstein, Appl. Phys. A **34** (1984) 73.

[Br78] J. Q. Broughton, and L. V. Woodcock, J. Phys. C **11** (1978) 2743.

[Br83a] J. Q. Broughton, and G. H. Gilmer, J. Chem. Phys. **79** (1983) 5105.

[Br83b] J. Q. Broughton, and G. H. Gilmer, J. Chem. Phys. **79** (1983) 5119.

[Ch80] C. T. Chang, L. W. Jørgensen, P. Nielsen and L. L. Lengyel, Nucl. Fus. **20** (1980) 859.

[Do64] B. Domeij, F. Brown, J. A. Davies, and M. McCarco, Can. J. Phys. **42** (1964) 1624.

[Er65] C. Erginsoy, G. H. Vineyard, and A. Shimizu, Phys. Rev. **139** (1965) A118.

[Fe47] E. Fermi and E. Teller, Phys. Rev. **72** (1947) 399.

[Fi74] H. J. Fitting, Phys. Status. Solidi **26** (1974) 525.

[Fl78] M. J. Fluss, L. C. Smedskjaer, M. K. Chason, D. G. Legnini, and R. W. Siegel, Phys. Rev. B **17** (1978) 3444.

[Fr76] S. Fraga, K. M. S. Saxena, and J. Karwowski, Handbook of Atomic Data (Elsevier, New York, 1976).

[Fr85] J. W. M. Frenken and J. F. van der Veen, Phys. Rev. Lett. **54** (1985) 134.

[Fr86] J. W. M. Frenken, P. M. J. Marée, and J. F. van der Veen, Phys. Rev. B **34** (1986) 7506.

[Ga76] Gas Encyclopaedia (Division Scientifique de l'Air Liquide/Elsevier, Amsterdam, 1976).

[Gi59] L. A. Girifalco and V. G. Weiser, Phys. Rev. **114** (1959) 687.

[Gra65] I. S. Gradshteyn and I. M. Ryhzik, Table of Integrals, Series and Products (Academic Press, New York, 1965).

[Gry65] M. Gryzinski, Phys. Rev. A **138** (1965) 305, 322 and 336.

[Gr57] A. E. Grün, Naturforsch. Teil A **12** (1957) 89.

[Gu76] O. Gunnarsson and B. I. Lundqvist, Phys. Rev. B **13** (1976) 4274.

[Ha79] P. Hautojärvi (ed.), Positrons in Solids, Topics in Current Physics **12** (Springer, Berlin, 1979).

[Ha83] H. E. Hansen and U. Ingerslev–Jensen, J. Phys. D **16** (1983) 1353.

[Ha83a] D. E. Harrison, Jr., Radiat. Eff. **70** (1983) 1.

[Ha83b] D. E. Harrison, Jr. and R. P. Webb, Nucl. Instr. Meth. **218** (1983) 727.

[He76] K. F. J. Heinrich, D. E. Newbury and H. Yakowitz (eds.), Use of the Monte Carlo Calculations in Electron Probe Microanalysis and Scanning Electron Microscope (US Govt. Print. Off., Washington, 1976).

[Ho85] P. S. Ho, T. Kwok, T. Nguyen, C. Nitta, and S. Yip, Scripta Metallurgica **19** (1985) 993.

[Ho64] P. Hohenberg and W. Kohn, Phys. Rev. **136** (1964) 864.

[Ic80] S. Ichimura, K. Aramata, and R. Shimizu, J. Appl. Phys. **30** (1980) 2853.

[Ic81] S. Ichimura and R. Shimizu, Surf. Science **112** (1981) 386.

[Is74] T. Ishitani and R. Shimizu, Phys. Lett. **46A** (1974) 487.

[IC84] ICRV–Rep. 37, Stopping powers for electrons and positrons (ICRV, Publications, 7910 Woodmont Avenue, Bethesda, MD 20814, USA, 1984).

[Ja86] M. M. Jakas and D. E. Harrison, Jr., Nucl. Instr. Meth. **B14** (1986) 535.

[Ja85] C. S. Jayanthi, E. Tosatti, and L. Pietronero, Phys. Rev. B **31** (1985) 3456.

[Jo83] R. E. Johnson and W. L. Brown, Nucl. Instr. Meth. **209/210** (1983) 469.

[Ka82] J. Kalef Ezra, Y. S. Horowitz, and J. M. Mack, Nucl. Instr. Meth. **195** (1982) 587.

[Ka59] I. R. Kanicheva and V. A. Burtsev, Fizika Tverdogo Tela **1** (1959) 1250.

[Ki71] C. Kittel, Introduction to Solid State Physics (Wiley, New York, 1971).

[Ko65] W. Kohn and L. J. Sham, Phys. Rev. A **140** (1965) 1133.

[La61] N. Laegreid and G. K. Wehner, J. Appl. Phys. **32** (1961) 365.

[La86] U. Landman, W. D. Luedtke, R. N. Barnett, C. L. Cleveland, M. W. Ribarsky, E. Arnold, S. Ramesh, H. Baumgart, A. Martinez, and B. Khan, Phys. Rev. Lett. **56** (1986) 155.

[Li82] R. Lipowsky, Phys. Rev. Lett. **49** (1982) 1575.

[Li84] R. Lipowsky, J. Appl. Phys. **55** (1984) 2485.

[Li86] R. Lipowsky, Phys. Rev. Lett. **57** (1986) 2876.

[Ma60] A. F. Makhov, Sov. Phys. Solid State **2** (1960) 1934, 1942, and 1945.

[Me63] E. Merzbacher, Quantum Mechanics (Wiley, New York, 1963).

[Mi82a] A. P. Mills, Jr., in "Proc. LXXXIII Intern. School of Physics "Enrico Fermi"", eds. W. Brandt and A. Dupasquier (Academic Press, New York, 1982).

[Mi82b] A. P. Mills and R. J. Wilson, Phys. Rev. B **26** (1982) 490.

[Mi81] S. L. Milora, J. Fus. Energy **1** (1981) 15.

[Mi84] R. Miranda and J. M. Rojo, Vacuum **34** (1984) 1069.

[Mo87] S. G. J. Mochrie, Phys. Rev. Lett. **59** (1987) 304.

[Mä86] J. Mäkinen, A. Vehanen, P. Hautojärvi, H. Huomo, J. Lahtinen, R. M. Nieminen and S. Valkealahti, Surf. Sci. **175** (1986) 385.

[Na62] J. Naghizadeh and S. A. Rice, J. Chem. Phys. **36** (1962) 2710.

[Ni85] B. Nielsen, K. G. Lynn, A. Vehanen and P. J. Schultz, Phys. Rev. B **32** (1985) 2296.

[Ni82] H. Niedrig, J. Appl. Phys. **53** (1982) R15.

[Ni80] R. M. Nieminen and J. Oliva, Phys. Rev. B **22** (1980) 2226.

[Ni59] B. P. Nigam, M. K. Sundaresan, and Ta-You Wu, Phys. Rev. **115** (1959) 491.

[No73] C. Nordling, Fysik Handbok (Almqvist Wiksell, Stockholm, 1973).

[Oe73] H. Oechsner, Z. Physik **261** (1973) 37.

[Po85] V. Pontikis, and V. Rosato, Surf. Sci. **162** (1985) 150.

[Pu83] M. J. Puska and R. M. Nieminen, Phys. Rev. B **27** (1983) 6121.

[Ra64] A. Rahman, Phys. Rev. **136** (1964) 405.

[Ro81] M. T. Robinson, in "Sputtering By Particle Bombardment I", ed. R. Behrisch, Topics in Applied Physics **47** (Springer, 1981) p. 73.

[Ro54] F. Rohrlich and B. C. Carlson, Phys. Rev. **93** (1954) 38.

[Ro86] V. Rosato, G. Ciccotti, and V. Pontikis, Phys. Rev. B **33** (1986) 1860.

[Sc85] W. Schommers, Phys. Rev. B **32** (1985) 6845.

[Sc78] J. Schou and H. Sørensen, J. Appl. Phys. **49** (1978) 816.

[Se55] H. H. Seliger, Phys. Rev. **100** (1955) 1029.

[Sh85] M. H. Shapiro, P. K. Haff, T. A. Tombrello, D. E. Harrison, Jr., and R. P. Webb, Radiat. Eff. **89** (1985) 234.

[Sh83] R. Shimizu and S. Ichimura, Surf. Sci. **133** (1983) 250.

[Si86] J. Sielanko and W. Szyszko, Nucl. Instr. Meth. B **16** (1986) 340.

[Si75] P. Sigmund, in "Radiation damage processes in materials", ed. C. H. S. Dupuy (Nordhoff, Leiden, 1975) p. 3.

[Sp59] L. V. Spencer, Nat. Bur. Stand. Monogr. **1** (1959) 1.

[St62] R. V. Stuart and G. K. Wehner, J. Appl. Phys. **33** (1962) 2345.

[Sø78a] H. Sørensen and J. Schou, J. Appl. Phys. **49** (1978) 5311.

[Sø78b] H. Sørensen and J. Schou, J. Nucl. Mat. **76&77** (1978) 634.

[To83] T. A. Tombrello, in "Desorption Induced by Electronic Transitions", DIET 1, eds. N. H. Tolk, M. M. Traum, J. C. Tully and T. E. Madey (Springer, Berlin, 1983) p. 239.

[Va83] S. Valkealahti and R. M. Nieminen, Appl. Phys. A **32** (1983) 95.

[Va84] S. Valkealahti and R. M. Nieminen, Appl. Phys. A **35** (1984) 51.

[Va70] C. Varelas and J. Biersack, Nucl. Instr. Meth. **79** (1970) 213.

[Ve80] A. van Veen and J. M. Fluit, Nucl. Instr. Meth. **170** (1980) 341.

[Ve82] A. van Veen, W. Th. M. Buters, G. J. van der Kolk and L. M. Caspers, Nucl. Instr. Meth. **194** (1982) 485.

[Ve85] A. Vehanen, J. Mäkinen, P. Hautojärvi, H. Huomo, J. Lahtinen, R. M. Nieminen and S. Valkealahti, Phys. Rev. B **32** (1985) 7561.

[Ve87] A. Vehanen, K. Saarinen, P. Hautojärvi, and H. Huomo, Phys. Rev. B **35** (1987) 4606.

[Ve67] L. Verlet, Phys. Rev. **159** (1967) 98.

[Vy58] A. Ya. Vyatskin and A. F. Makhov, Sov. Phys. – Tech. Phys. **3** (1958) 690.

[Vy67] A. Ya. Vyatskin and V. V. Trunev, Radio Eng. Electron. Phys. **9** (1967) 1526.

[Vy73a] A. Ya. Vyatskin and V. V. Trunev, and Kh. I. Fitting, Radio Eng. Electron. Phys. **18** (1973) 157.

[Vy73b] A. Ya. Vyatskin and V. V. Trunev, and Kh. I. Fitting, Radio Eng. Electron. Phys. **18** (1973) 1238.

[Vy76] A. Ya. Vyatskin and V. Yu. Khramov, Radio Eng. Electron. Phys. **21** (1976) 107.

[Vy77] A. Ya. Vyatskin, A. N. Kabanov, B. N. Smirnov, and V. Yu. Khramov, Sov. Phys. Solid State **19** (1977) 157.

[Wea83] R. C. Weast (ed.), Handbook of Chemistry and Physics (CRC Press, Ohio, 1983-84).

[Web83] R. P. Webb and D. E. Harrison, Jr., Nucl. Instr. Meth. **218** (1983) 697.

[We67] C. H. Weijsenfeld, Philips Res. Repts Suppl. No. 2 (1967).

[Zi85] J. F. Ziegler, J. P. Biersack and U. Littmark, The Stopping and Ranges of Ions in Matter, vol. 1, ed. J. F. Ziegler (Pergamon, New York, 1985).

[Zo84] A. Zomorrodian, S. Tougaard and S. Ignatiev, Phys. Rev. B **30** (1984) 3124.

[Zh86] D.-M. Zhu and J. G. Dash, Phys. Rev. Lett. **57** (1986) 2959.

[Øh85] M. Øhlenschlaeger, H. H. Andersen, J. Schou and H. Sørensen, Rad. Prot. Dosimetry **13** (1985) 61.